



**HAL**  
open science

## **A Mars 2020 Perseverance SuperCam Perspective on the Igneous Nature of the Máaz formation at Jezero crater and link with Séítah, Mars**

A. Udry, A. Ostwald, V. Sautter, A. Cousin, O. Beyssac, O. Forni, G. Dromart, K. Benzerara, M. Nachon, B. Horgan, et al.

### ► **To cite this version:**

A. Udry, A. Ostwald, V. Sautter, A. Cousin, O. Beyssac, et al.. A Mars 2020 Perseverance SuperCam Perspective on the Igneous Nature of the Máaz formation at Jezero crater and link with Séítah, Mars. *Journal of Geophysical Research. Planets*, 2023, The MARS Perseverance Rover Jezero Crater Floor Campaign, 128 (7), pp.e2022JE007440. 10.1029/2022JE007440 . hal-04044819

**HAL Id: hal-04044819**

**<https://hal.science/hal-04044819v1>**

Submitted on 1 Nov 2023

**HAL** is a multi-disciplinary open access archive for the deposit and dissemination of scientific research documents, whether they are published or not. The documents may come from teaching and research institutions in France or abroad, or from public or private research centers.

L'archive ouverte pluridisciplinaire **HAL**, est destinée au dépôt et à la diffusion de documents scientifiques de niveau recherche, publiés ou non, émanant des établissements d'enseignement et de recherche français ou étrangers, des laboratoires publics ou privés.

Special Section:

The Mars Perseverance Rover Jezero Crater Floor Campaign

Key Points:

- The Mááz formation in Jezero crater consists of basaltic to basaltic-andesite lava flows likely originating from the same parental magma
- The Mááz formation shows various igneous textures and has a different magmatic history than the other known Martian igneous rocks
- The study of samples from the Mááz formation on Earth will help constrain the Martian cratering chronology and Martian igneous evolution

Supporting Information:

Supporting Information may be found in the online version of this article.

Correspondence to:

A. Udry,  
arya.udry@unlv.edu

Citation:

Udry, A., Ostwald, A., Sautter, V., Cousin, A., Beyssac, O., Forni, O., et al. (2023). A Mars 2020 *Perseverance* SuperCam perspective on the igneous nature of the Mááz formation at Jezero crater and link with Séítah, Mars. *Journal of Geophysical Research: Planets*, 128, e2022JE007440. <https://doi.org/10.1029/2022JE007440>

Received 23 JUN 2022  
Accepted 17 OCT 2022  
Corrected 31 JUL 2023

This article was corrected on 31 JUL 2023. See the end of the full text for details.

Author Contributions:

Conceptualization: P. Beck

## A Mars 2020 *Perseverance* SuperCam Perspective on the Igneous Nature of the Mááz Formation at Jezero Crater and Link With Séítah, Mars

A. Udry<sup>1</sup> , A. Ostwald<sup>1</sup>, V. Sautter<sup>2</sup>, A. Cousin<sup>2</sup> , O. Beyssac<sup>3</sup>, O. Forni<sup>2</sup>, G. Dromart<sup>4</sup>, K. Benzerara<sup>5</sup>, M. Nachon<sup>6</sup> , B. Horgan<sup>7</sup> , L. Mandon<sup>8</sup> , E. Clavé<sup>9</sup> , E. Dehouck<sup>4</sup> , E. Gibbons<sup>10</sup>, S. Alwmark<sup>11,12</sup> , E. Ravanis<sup>13</sup>, R. C. Wiens<sup>7,14</sup> , C. Legett<sup>14</sup> , R. Anderson<sup>15</sup> , P. Pilleri<sup>2</sup> , N. Mangold<sup>16</sup> , M. Schmidt<sup>17</sup> , Y. Liu<sup>18</sup>, J. I. Núñez<sup>19</sup> , K. Castro<sup>20</sup>, J. M. Madariaga<sup>20</sup> , T. Kizovski<sup>17</sup>, P. Beck<sup>21</sup>, S. Bernard<sup>3</sup> , T. Bosak<sup>22</sup> , A. Brown<sup>23</sup> , S. Clegg<sup>14</sup> , E. Cloutis<sup>10</sup> , B. Cohen<sup>24</sup>, S. Connell<sup>7</sup>, L. Crumpler<sup>25</sup> , V. Debaille<sup>26</sup>, D. Flannery<sup>27</sup> , T. Fouchet<sup>8</sup> , T. S. J. Gabriel<sup>15</sup>, O. Gasnault<sup>2</sup> , C. D. K. Herd<sup>28</sup> , J. Johnson<sup>19</sup> , J. A. Manrique<sup>29</sup> , S. Maurice<sup>2</sup>, F. M. McCubbin<sup>30</sup>, S. McLennan<sup>31</sup> , A. Ollila<sup>14</sup>, P. Pinet<sup>2</sup> , C. Quantin-Nataf<sup>4</sup>, C. Royer<sup>8</sup> , S. Sharma<sup>13</sup>, J. I. Simon<sup>30</sup> , A. Steele<sup>32</sup> , N. Tosca<sup>33</sup> , A. Treiman<sup>34</sup> , and the SuperCam team

<sup>1</sup>Department of Geosciences, University of Nevada Las Vegas, Las Vegas, NV, USA, <sup>2</sup>CNRS, Institut de Recherche en Astrophysique et Planétologie, Université de Toulouse 3 Paul Sabatier, CNES, Toulouse, France, <sup>3</sup>CNRS UMR 7590, Institut de Minéralogie, de Physique des Matériaux et de Cosmochimie, Sorbonne Université, Muséum National d'Histoire Naturelle, Paris, France, <sup>4</sup>LGL-TPE, CNRS, Université de Lyon, UCBL, ENSL, Lyon, France, <sup>5</sup>CNRS, Université Denis Diderot, Paris, France, <sup>6</sup>Department of Geology and Geophysics, Texas A&M University, College Station, TX, USA, <sup>7</sup>Earth, Atmospheric, and Planetary Sciences, Purdue University, West Lafayette, IN, USA, <sup>8</sup>LESIA, Observatoire de Paris, CNRS, Université PSL, Sorbonne Université, Université de Paris, Meudon, France, <sup>9</sup>CELIA, CNRS, Université de Bordeaux, CEA, Talence, France, <sup>10</sup>Department of Geography, University of Winnipeg, Winnipeg, MB, Canada, <sup>11</sup>Niels Bohr Institute, University of Copenhagen, Copenhagen, Denmark, <sup>12</sup>Department of Geology, Lund University, Lund, Sweden, <sup>13</sup>Hawai'i Institute of Geophysics and Planetology, University of Hawai'i, Honolulu, HI, USA, <sup>14</sup>Los Alamos National Laboratory (LANL), Los Alamos, NM, USA, <sup>15</sup>U. S. Geological Survey Astrogeology Science Center, Flagstaff, AZ, USA, <sup>16</sup>Laboratoire de Planétologie et Géodynamique, CNRS UMR 6112, Université de Nantes, Université d'Angers, Nantes, France, <sup>17</sup>Department of Earth Sciences, Brock University, St. Catharines, ON, Canada, <sup>18</sup>Jet Propulsion Laboratory, California Institute of Technology, Pasadena, CA, USA, <sup>19</sup>Johns Hopkins University Applied Physics Laboratory, Laurel, MD, USA, <sup>20</sup>Department of Analytical Chemistry, University of the Basque Country UPV/EHU, Leioa, Spain, <sup>21</sup>Université Grenoble Alpes, Grenoble, France, <sup>22</sup>Department of Earth, Atmospheric and Planetary Sciences, Massachusetts Institute of Technology, Cambridge, MA, USA, <sup>23</sup>Plancius Research, Severna Park, MD, USA, <sup>24</sup>NASA Goddard Space Flight Center, Greenbelt, MD, USA, <sup>25</sup>New Mexico Museum of Natural History & Science, Albuquerque, NM, USA, <sup>26</sup>Laboratoire G-Time, Université Libre de Bruxelles, Brussels, Belgium, <sup>27</sup>Queensland University of Technology, Brisbane, QLD, Australia, <sup>28</sup>Department of Earth and Atmospheric Sciences, University of Alberta, Edmonton, AB, Canada, <sup>29</sup>Unidad Asociada UVA-CSIC-CAB, University of Valladolid (UVA), Valladolid, Spain, <sup>30</sup>NASA Johnson Space Center, Astromaterials Research and Exploration Science Division, Houston, TX, USA, <sup>31</sup>State University of New York (SUNY) Stony Brook, New York, NY, USA, <sup>32</sup>Earth and Planets Laboratory, Carnegie Institution for Science, Washington, DC, USA, <sup>33</sup>Department of Earth Sciences, University of Oxford, Oxford, UK, <sup>34</sup>Lunar and Planetary Institute, Houston, TX, USA

**Abstract** The Mááz formation consists of the first lithologies in Jezero crater analyzed by the Mars 2020 *Perseverance* rover. This formation, investigated from Sols (Martian days) 1 to 201 and from Sols 343 to 382, overlies the Séítah formation (previously described as an olivine-rich cumulate) and was initially suggested to represent an igneous crater floor unit based on orbital analyses. Using SuperCam data, we conducted a detailed textural, chemical, and mineralogical analyses of the Mááz formation and the Content member of the Séítah formation. We conclude that the Mááz formation and the Content member are igneous and consist of different lava flows and/or possibly pyroclastic flows with complex textures, including vesicular and non-vesicular rocks with different grain sizes. The Mááz formation rocks exhibit some of the lowest Mg# (=molar 100 × MgO/MgO + FeO) of all Martian igneous rocks analyzed so far (including meteorites and surface rocks) and show similar basaltic to basaltic-andesitic compositions. Their mineralogy is dominated by Fe-rich augite to possibly ferrosilite and plagioclase, and minor phases such as Fe-Ti oxides and Si-rich phases. They show a broad diversity of both compositions and textures when compared to Martian meteorites and other surface rocks. The different Mááz and Content lava or pyroclastic flows all originate from the same parental magma and/or the same magmatic system, but are not petrogenetically linked to the Séítah formation. The study of returned Mááz

samples in Earth-based laboratories will help constrain the formation of these rocks, calibrate Martian crater counting, and overall, improve our understanding of magmatism on Mars.

**Plain Language Summary** The Mars 2020 *Perseverance* rover landed on Mars in the Jezero crater on 18 February 2021. The main goals of this mission are to constrain the geology of the Jezero crater and its delta, to search for biosignatures (evidence of ancient life), to sample rocks to return to Earth, and to prepare for human exploration. Here we study the rock formation observed at the landing site, named the Mááz formation. We conclude that this rock formation is igneous (=formed from cooling and crystallization of lava or magma) consisting of iron-rich basaltic lava flows, formed through effusive (i.e., outpouring of lava without explosions) volcanism. When compared to other Martian magmatic rocks, these rocks show a large variety of textures (shape and size of minerals) and compositions, making them different from the Martian magmatic rocks studied so far. The various lava flows of the Mááz rocks are likely all related, but not related to the underlying Séítah rock formation. *Perseverance* has collected core samples from the Mááz and Séítah rocks that could be among the Martian rocks to be returned to Earth in the 2030s. Their study in Earth-based laboratories will allow us to better understand the evolution of Martian magmatism.

## 1. Introduction

### 1.1. Broad Scale Geological Context

The Mars 2020 *Perseverance* rover landed in Jezero crater on 18 February 2021, in the Octavia E. Butler (OEB) landing site in the unit previously called Crater floor-fractured rough (Cf-fr) unit as determined from orbital observations. The portion explored by *Perseverance* is now called the Mááz (“Mars” in Navajo) formation (fm; e.g., Goudge et al., 2015; Horgan et al., 2020). This unit, also previously described as the mafic floor, has had a range of proposed origins, including igneous, such as lava or pyroclastic flows (Brown et al., 2010, 2020; Goudge et al., 2015; Hamilton & Christensen, 2005; Horgan et al., 2020); impact (e.g., Mustard et al., 2007); or possibly aeolian or fluvio-lacustrine sedimentary (Horgan et al., 2020; Stack et al., 2020). We use the terminology from Stack et al. (2020; see Farley et al. (2022), and Wiens et al. (2022), for the broader context of the Jezero crater floor).

In this study, we focus on the Mááz fm, which was explored by *Perseverance* from Sols (Martian days of the mission) 1 to 201 and from Sols 343 until Sol 382 (Figure 1), to constrain the nature and origin of this formation using data from the SuperCam instrument (Figure 1), as also described in Wiens et al. (2022). We also study the Content member (mb), which overlies the Séítah (“amongst the dunes” in Navajo) fm, but is compositionally and mineralogically more similar to the Mááz fm (Beyssac et al., 2023; Nuñez et al., 2022). The Séítah fm was investigated from Sol 202 to 342 (with additional analyses on targets Entrevaux on Sol 173, and Aiguines on Sol 178 and three targets analyzed in NW Séítah on Sols 417–420) and was found to be consistent with an olivine-rich cumulate lithology (Liu et al., 2022; Wiens et al., 2022). Although the stratigraphic location of the Content mb in the Mááz fm is unclear, we show below that the composition of this member supports the hypothesis that Content is part of the Mááz fm. The dark-toned crater floor in Jezero (i.e., Cf-fr), including the Mááz fm and Content mb, have different estimated ages of ~2.6 Ga up to 3.6 Ga from orbital observations and crater counting, according to Goudge et al. (2015) and Shahrzad et al. (2019). The study of the Mááz fm and Content mb, if igneous, is critical to better understand the magmatic history of Mars and its magmatic diversity through time, since we do not have any Martian meteorite of this age (e.g., Udry et al., 2020: most meteorites are younger than 2.4 Ga, in addition to two samples or with clasts older than 4.1 Ga). Furthermore, because the Mááz fm has a defined crater retention age, geochronology of returned samples from the Mááz fm would contribute to refining the existing Martian crater counting calibration.

### 1.2. SuperCam Investigations

SuperCam is a remote science instrument that measures rock chemistry with Laser-Induced Breakdown Spectroscopy (LIBS), mineralogy with Raman and Visible and Infrared reflectance spectroscopy (VISIR), and textures using the Remote Micro Imager (RMI; see Maurice et al. (2021) and Wiens et al. (2021), for details on the instrument and techniques, also described here in Section 2). The small LIBS beam size (~170–370  $\mu\text{m}$ , depending on the distance from the rover to target) allows for measurements of individual grains or microstructural components

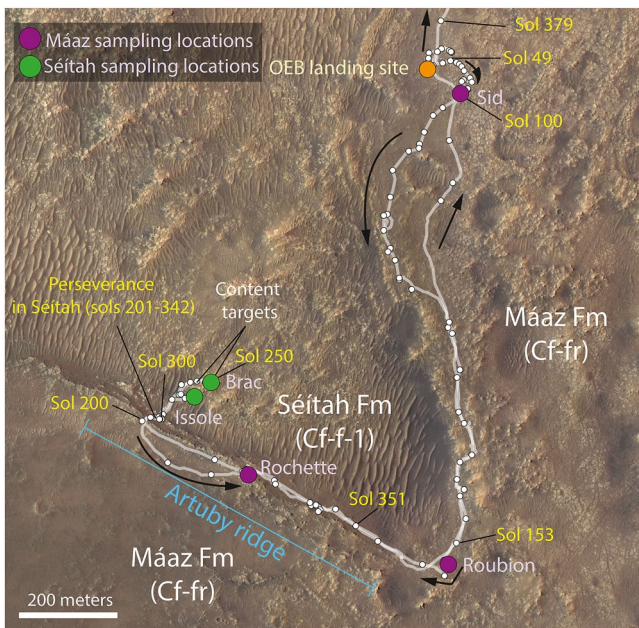


**Figure 1.** Map of the Mááz and Séítah formation, each point indicates the different stops of the *Perseverance* rover. *Perseverance* explored the Mááz fm from Sol 1 to Sol 201 and from Sol 343 to Sol 379 and the Séítah fm from Sol 202 to Sol 342. We indicate the locations of the rover ~ every 50 Sols. The core sampling locations are shown in purple and the Octavia E. Butler landing site (OEB) in orange. The black arrows represent the direction of the traverse of *Perseverance*. The Content targets have been represented. No rock core was sampled at the Roubion location, due to sample disintegrating during sampling (Farley et al., 2022). Montedenier (Sol 190) and Montagnac (Sol 196) rock cores were samples at the Rochette location; Salette (Sol 262) and Coulettes (Sol 271) rock cores were samples at the Brac location; Robine (Sol 295) and Montagnac (Sol 337) rock cores were samples at the Issole location; and Hahonih (Sol 371) and Atsah (Sol 377) rock cores were samples at the Sid location.

of targets with large enough grains (e.g., Maurice et al., 2021). Through fast analyses and frequent use, SuperCam allows for the collection of representative rock compositions and textures throughout the whole traverse in Jezero crater. SuperCam measured a total of 231 of targets (=rasters) in the Mááz fm (including long distance targets, >6.5 m), with a total of 114 non-abraded rock targets (in contrast to abraded rock surfaces and soil targets) via LIBS, all measured at a distance less than 6.5 m from the rover (Tables S1 and S2). In the Mááz fm, the rover was used to perform four abrasions at targets Guillaumes (Sols 162, 163, 166, and 168), Bellegarde (Sols 187, 188, and 191), Montpezat (Sol 350), and Alfalfa (Sols 371 and 379). Samples were successfully collected from the rocks corresponding to the Bellegarde and Alfalfa abrasion patches for sample return. SuperCam LIBS analyses were acquired on 11 of these Mááz abraded targets. The Content mb includes a total of six non-abraded targets analyzed by LIBS and measured at 6.5 m or closer (Table S1), but no abraded targets.

## 2. Methods

### 2.1. SuperCam Techniques and Datasets

The SuperCam instrument includes a LIBS, VISIR spectrometers, RMI, Raman, Luminescence, and a microphone (MIC), the latter not described here.

#### 2.1.1. LIBS

The LIBS instrument uses a pulsed 1,064 nm laser creating a plasma from the target rock or soil, from 1.5 to ~11 m, with a laser beam of ~170  $\mu\text{m}$  diameter at 2.4 m that increases to ~370  $\mu\text{m}$  at 5.5 m (see Maurice et al., 2021; Wiens et al., 2021 for references to SuperCam instrument characteristics). With such small beam sizes, coarse-grained minerals can sometimes be analyzed without signal mixing among mineral grains. The plasma light is collected and analyzed between 245 and 853 nm, with a field of view (FOV) of ~0.8 mrad. The LIBS spectrum consists of 7933 channels, and elements are identifiable by different emission lines. Each target is analyzed in a column  $\times$  grid or line pattern referred to as a raster (3  $\times$  3, 10  $\times$  1, 1  $\times$  5, and 2  $\times$  2; Maurice et al., 2021). On each point of such raster, a typical observation consists of

30 laser shots, allowing for depth profile composition analyses. For each point analysis, the first five shots are removed from the calculations as they are inferred to represent the dust layer present on most Martian targets (Maurice et al., 2021). When multiple techniques are used along the raster, LIBS analyses are usually conducted before visible and Infrared (VISIR) spectroscopy, as the plasma expansion removes dust from the targets surface. Twenty three SuperCam LIBS calibration targets (SCCT) are present on board the rover and comprise six single igneous mineral compositions, which are homogeneous and monomineralic targets (orthoclase, andesine, olivine Fo<sub>65</sub>, diopside, Mg-enstatite and ferro-hypersthene), synthetic glassy basaltic targets doped with minor elements (such as developed for ChemCam on board the Curiosity rover; Fabre et al., 2011), and several targets simulating typical rock compositions (Cousin et al., 2022; Manrique et al., 2020). During the exploration of the Mááz fm, 115 observations on SCCT were made. The SCCT are analyzed every 2 months in order to verify that the quantitative models (developed to quantify the Mars targets) remain accurate, as the chemistry of these LIBS calibration targets is very well defined. Here we used the major-element oxide composition (MOC) calibration defined by Anderson et al. (2022) that uses a suite of 1198 laboratory spectra of 334 well-characterized reference samples. The SuperCam team has developed quantitative calibration models for the major element oxides SiO<sub>2</sub>, TiO<sub>2</sub>, Al<sub>2</sub>O<sub>3</sub>, FeO<sub>T</sub>, MgO, CaO, Na<sub>2</sub>O, and K<sub>2</sub>O (Anderson et al., 2022) using a lab database made of a suite of 1198 laboratory spectra of 334 well-characterized reference samples, containing the SCCT as well. In order to refine these quantitative models, the frequency of SCCT measurements during the first months on Mars was higher. The LIBS technique also reports detection of Rb, Sr, Ba, Cr, Cu, F, Mn, Zn, H, S, and Cl (Anderson et al., 2022; Maurice et al., 2021).

Specific criteria were applied to select LIBS data to ensure accurate data, including distance (<6.5 m; long distance analyses result in different laser energies at the targets, affecting MOC determination), focus (two consecutive autofocus fit curves performed during a raster should be separated by less than 18 steps of the focus motor stage), and intensity ( $>10^{14}$  photons/pulse/mm<sup>2</sup>/sr/nm at the source, the opposite representing poor laser-target coupling with inefficient ablation). As we are focusing on primary compositions, we also removed points with low MOC totals (<80 wt.%), which would indicate non-characterized chemical species (e.g., OH, SO<sub>4</sub><sup>2-</sup>, CO<sub>3</sub><sup>2-</sup>), likely associated with secondary phases. Laser-Induced Breakdown Spectroscopy observations of holes in rocks or past the hole edges were removed. We expect matrix effects for tailings and borehole observations: the laser-target coupling is strongly affected by the surface characteristics of the target, including hardness, absorptivity, and roughness, resulting in non-linear variations in the emission spectra. These physical matrix effects are expected to be especially significant for non-compact, fine-grained material, such as tailings, in which the shockwave caused by ablation may create significant (mm-size) pits with just a few laser shots. In total, 1057 reliable observation points were used by LIBS for the Máaz fm (720 points for non-abraded surfaces, 101 soils, 61 abraded surfaces, 60 borehole and tailings, and 115 SCCT analyses) and 45 points for non-abraded surfaces in the Content mb. All SuperCam LIBS targets are described in Tables S1 (MOC compositions) and Table S2 (targets descriptions).

### 2.1.2. RMI

The RMI provides visible color images (using RGB filters) from 1 m to infinity with a FOV of 19 mrad and an angular optical resolution of 80  $\mu$ rad (Maurice et al., 2021). The RMI images provide for textural context for the LIBS, VISIR, and Raman data collected at different positions along the raster. The RMI mosaics presented here use a fusion technique to improve their quality. However, LIBS pits and dust clearing can still be visible at times and affect the natural appearance of the rock surfaces at a very local scale.

### 2.1.3. VISIR

The VISIR spectrometers are used to infer primary and secondary minerals (we focus on primary minerals in this study) from 1 m to infinity. The VIS wavelengths from 0.39–0.85  $\mu$ m (VIS) are used to constrain the mineralogy of several Fe-bearing minerals, whereas IR wavelengths range from 1.3 to 2.6  $\mu$ m (Fouchet et al., 2022; Maurice et al., 2021) and are used to identify Fe-bearing minerals, sheet silicates, sulfates, carbonates, organic compounds, molecular water, and H<sub>2</sub>O-bearing salts.

Time Resolved Raman (TRR) and Luminescence (TRL) are vibrational spectroscopy techniques with TRR irradiance of 10 and 30 kW/mm<sup>2</sup> per pulse with the green laser, at distances from 1.5 to 7 m. SuperCam's Raman shift ranges from 150 cm<sup>-1</sup> to >4,000 cm<sup>-1</sup> (Maurice et al., 2021; Wiens et al., 2021). Raman spectra can be used to identify major minerals and some organics. The TRL 532 nm laser can excite various emission centers in many minerals, such as carbonates, phosphates, zircons, and organics (Maurice et al., 2021).

## 2.2. Thermodynamic Modeling

To constrain the links between the different Máaz fm members and Content mb, we ran fractional crystallization models using the thermodynamic modeling software MELTS, already commonly used for Martian compositions (Balta & McSween, 2013; Baratoux et al., 2011; Basu Sarbadhikari et al., 2011; McSween, Ruff, et al., 2006; McSween, Wyatt, et al., 2006; Monders et al., 2007; Ostwald et al., 2022; Peslier et al., 2010; Symes et al., 2008; Taylor et al., 2002; Udry, Balta et al., 2014; Udry, Lunning, et al., 2014; Udry et al., 2018). Models were conducted using the Rhyolite-MELTS thermodynamic phase equilibria calculator, version 1.0.2, which best replicates systems below pressures of 2.0 GPa (Ghiorso & Gualda, 2015; Gualda et al., 2012). We used a temperature decrease in decrements of 10°C and initial temperature of 1700°C, significantly above the liquidus.

Initial compositions selected for modeling included the averaged LIBS compositions of the Content mb, the lower Máaz mb, and the fine-grained (<1 mm) and the coarser-grained (>1 mm) upper Máaz mb (Table 1). Importantly, MELTS calculations normalize all bulk composition totals to 100 wt.%, so all modeled oxide values are higher than the averages obtained by the rover.

We investigate various water contents, oxygen fugacities ( $f_{O_2}$ ), and pressures in these models. Water contents were varied in each model to include 0.07 wt.%, 0.50 wt.%, and 1.0 wt.% H<sub>2</sub>O. Constraints on volatile reservoirs in the Martian mantle range between 0 wt.% and 1.5 wt.% H<sub>2</sub>O, relevant for Martian compositions (e.g.,

**Table 1**  
*Compositions of Primary Non-Abraded Surface Targets Sorted by Textures in the Máaz fm and Content mb*

| Upper Máaz member   | SiO <sub>2</sub> | SiO <sub>2</sub> Stdev | TiO <sub>2</sub> | TiO <sub>2</sub> Stdev | Al <sub>2</sub> O <sub>3</sub> | Al <sub>2</sub> O <sub>3</sub> Stdev | FeO <sub>T</sub> | FeO <sub>T</sub> Stdev | MgO  | MgO Stdev | CaO  | CaO Stdev | Na <sub>2</sub> O | Na <sub>2</sub> O Stdev | K <sub>2</sub> O | K <sub>2</sub> O Stdev | Total | Mg# |  |
|---------------------|------------------|------------------------|------------------|------------------------|--------------------------------|--------------------------------------|------------------|------------------------|------|-----------|------|-----------|-------------------|-------------------------|------------------|------------------------|-------|-----|--|
| Mixed               | 46.6             | 2.40                   | 0.22             | 0.06                   | 7.83                           | 1.30                                 | 25.3             | 4.15                   | 1.72 | 0.70      | 4.38 | 0.66      | 2.79              | 0.34                    | 0.96             | 0.45                   | 89.8  | 11  |  |
| Very fine-grained   | 52.6             | 2.25                   | 0.93             | 0.20                   | 7.33                           | 1.19                                 | 16.2             | 4.20                   | 2.59 | 0.66      | 5.22 | 0.72      | 2.14              | 0.23                    | 0.92             | 0.34                   | 87.9  | 22  |  |
| Fine-grained        | 51.6             | 2.45                   | 0.81             | 0.12                   | 10.4                           | 1.27                                 | 15.2             | 3.05                   | 2.11 | 0.57      | 5.71 | 0.67      | 3.18              | 0.30                    | 1.42             | 0.37                   | 90.5  | 20  |  |
| Medium-grained      | 53.0             | 2.76                   | 0.50             | 0.08                   | 9.48                           | 1.29                                 | 16.7             | 3.49                   | 1.82 | 0.58      | 4.36 | 0.63      | 3.15              | 0.33                    | 1.51             | 0.44                   | 90.5  | 16  |  |
| Coarse-grained      | 50.2             | 2.96                   | 0.56             | 0.10                   | 8.53                           | 1.36                                 | 23.5             | 4.41                   | 2.79 | 0.74      | 5.28 | 0.73      | 2.70              | 0.32                    | 0.80             | 0.41                   | 94.4  | 17  |  |
| Av. Fine-grained    | 52.1             | 2.35                   | 0.87             | 0.16                   | 8.88                           | 1.23                                 | 15.7             | 3.62                   | 2.35 | 0.61      | 5.46 | 0.70      | 2.66              | 0.26                    | 1.17             | 0.35                   | 89.2  | 21  |  |
| Av. Coarser-grained | 51.6             | 2.86                   | 0.53             | 0.09                   | 9.01                           | 1.32                                 | 20.1             | 3.95                   | 2.31 | 0.66      | 4.82 | 0.68      | 2.92              | 0.32                    | 1.15             | 0.42                   | 92.5  | 17  |  |
| Lower Máaz mb       |                  |                        |                  |                        |                                |                                      |                  |                        |      |           |      |           |                   |                         |                  |                        |       |     |  |
| Fine-grained        | 44.3             | 2.18                   | 1.23             | 0.09                   | 5.84                           | 1.01                                 | 22.2             | 3.17                   | 4.06 | 0.78      | 9.62 | 0.84      | 2.28              | 0.26                    | 0.38             | 0.21                   | 89.9  | 25  |  |
| Coarse-grained      | 46.4             | 2.67                   | 0.41             | 0.09                   | 7.02                           | 1.25                                 | 20.2             | 2.87                   | 5.17 | 1.17      | 7.22 | 1.00      | 2.39              | 0.31                    | 0.41             | 0.40                   | 89.3  | 31  |  |
| Average             | 45.4             | 2.42                   | 0.82             | 0.09                   | 6.43                           | 1.13                                 | 21.2             | 3.02                   | 4.62 | 0.98      | 8.42 | 0.92      | 2.34              | 0.28                    | 0.39             | 0.30                   | 89.6  | 28  |  |
| Content mb          |                  |                        |                  |                        |                                |                                      |                  |                        |      |           |      |           |                   |                         |                  |                        |       |     |  |
| Fine-grained        | 50.1             | 3.00                   | 0.77             | 0.08                   | 11.4                           | 1.10                                 | 21.0             | 3.17                   | 2.02 | 0.42      | 3.11 | 0.65      | 3.83              | 0.40                    | 1.69             | 0.37                   | 93.9  | 15  |  |
| Medium-grained      | 56.9             | 2.52                   | 0.25             | 0.08                   | 14.5                           | 1.14                                 | 9.22             | 2.55                   | 1.38 | 0.39      | 3.19 | 0.56      | 4.77              | 0.37                    | 2.02             | 0.51                   | 92.2  | 21  |  |
| Average             | 53.5             | 2.76                   | 0.51             | 0.08                   | 12.9                           | 1.12                                 | 15.1             | 2.86                   | 1.70 | 0.40      | 3.15 | 0.61      | 4.30              | 0.38                    | 1.85             | 0.44                   | 93.0  | 17  |  |

McCubbin, Boyce, Srinivasan, et al., 2016; McCubbin, Boyce, Szabó, et al., 2016; Usui et al., 2015). Modeled  $fO_2$  was constrained at the fayalite-magnetite-quartz (FMQ) buffer, which is a value falling between melts in the lower Martian crust (FMQ-3) and estimates for the shallowly-formed Martian nakhlite meteorites (FMQ + 1.5) (e.g., Herd et al., 2002; Udry et al., 2020). Selected pressures include 1 atm (~1.02 bar, equivalent to Earth surface pressure), 1 kbar (~8 km depth) and 2 kbar (~16 km depth).

### 2.3. Chemometric Analysis

The Máaz SuperCam MOC values were analyzed by Principal Component (PC) Analysis (PCA) to see clusters and identify the possible presence of outliers, anomalous samples, etc. The PC represents factors that analyze multidimensional data and explain maximal variance among the samples. Each PC is a linear combination of the original variables. PCA allows a reduction of the number of variables, producing sample grouping and new variables (PC) that facilitate the comprehension of our data set.

Due to the fact that several points were analyzed for each target, the mean MOC value was calculated for each target. The data pre-processing was minimal, and the data were only mean-centered and mean-normalized for the clustering to be done based on the chemistry of the samples and not for different scale issues. The data set consisted of nine variables (SiO<sub>2</sub>, TiO<sub>2</sub>, Al<sub>2</sub>O<sub>3</sub>, FeO<sub>T</sub>, MgO, CaO, Na<sub>2</sub>O, K<sub>2</sub>O, and total content) and 130 targets, as well as nine SCCT. The samples belong to the upper and lower Máaz mbs and Content mb up to Sol 379.

## 3. Results

### 3.1. Geologic Context of Máaz

The rocks of the Máaz formation are geomorphologically variable, and descriptions range from structureless and massive to distinctly layered lithologies (e.g., Alwmark et al., 2023; Horgan et al., 2022; Núñez et al., 2022). The Máaz fm is divided into different members according to their geomorphology and spectral properties, as analyzed with the Mastcam-Z instrument (VNIR multispectral, stereoscopic imaging instrument; Crumpler et al., 2023; Horgan et al., 2022): Ch'al ("frog" in Navajo language—massive blocky hummocky rocks, east of OEB), Nataani and Roubion (polygonal, flat pavers south of OEB), Artuby (highstanding with recessive layers), and Rochette (capping unit). We describe the relationship between formations and members in Table 2. Artuby and Rochette were both found along the Artuby ridge, a 900 m ridge encountered from Sol 170 to 201 and from Sol 343 to 350

**Table 2**  
*Members of the Mááz Formation (See Horgan et al., 2023, for More Details)*

| Mááz formation            | Members  | Abraded patches |
|---------------------------|----------|-----------------|
| Upper Mááz fm             | Ch'al    | Alfalfa         |
|                           | Nataani  | –               |
| Transitional              | Roubion  | Guillaumes      |
| Lower Mááz fm             | Artuby   | Bellegarde      |
|                           | Rochette | –               |
| Directly overlying Séítah | Content  | –               |

Note. –: Not applicable.

(see Alwmark et al., 2023, for a thorough description of the Artuby ridge). In this study, we describe the Ch'al and Nataani mbs as the upper Mááz mb and the Artuby and Rochette mbs are both included in the lower Mááz mb. This is the same grouping as Wiens et al. (2022), who used the term “Mááz” for the upper Mááz mb and “Artuby” for lower Mááz mb, the observations of which were along Artuby ridge. Note that the Guillaumes and Alfalfa abrasion targets are located in the upper Mááz mb, and Bellegarde in the lower Mááz mb. The upper and lower Mááz terminologies used in this study follows Horgan et al. (2022), who grouped these members based on their spectral properties and morphology. Note that Roubion is likely transitional as it appears to be stratigraphically in between the upper and lower mbs according to Horgan et al. (2023). However, we grouped this member into the lower mb, as its composition is closest to the lower mb (see Section 3.2). In this study, the Content member was also included. The Content mb was investigated in the Séítah region (see Figure 1) and thus was not directly linked to the Mááz mb in the field (see Table S1 from Sols 239–280; Wiens et al. (2022)).

### 3.2. Textures Encountered in the Mááz Formation and Content mb

Here we define several textural groups within the rocks observed in the Mááz fm and the Content mb targets. We distinguish three main surface textures in the Mááz fm, including pitted, non-pitted (i.e., grained), and clotted/coated surface textures, all with varying grain sizes (Figure 2; including RMI with Gaussian color stretched images and MastCam-Z images). We use this simple classification as we can observe these textures for all RMI targets and as it allows for contextualizing and sorting LIBS chemical data. Color was not diagnostic to distinguish the different rocks in the Mááz fm, in contrast to igneous Gale crater rock classification (Sautter et al., 2014).

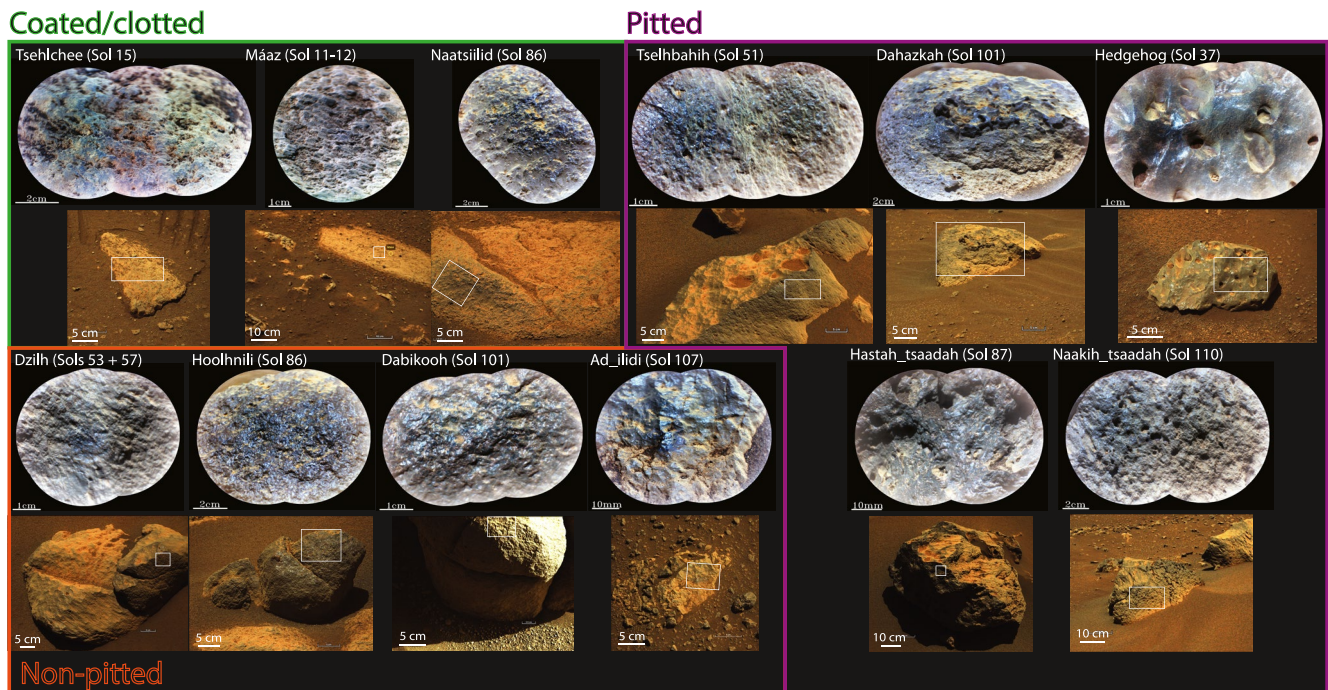


**Figure 2.** Remote Micro Imager (upper mosaics) with Gaussian color stretching images and Mastcam-Z images (lower images with white frames showing the RMI location) of different textures encountered in the Mááz fm: 1) Coated/clotted: Tselhchee (Sol 15, very fine-grained); Mááz (Sol 11–12, very fine-grained), and Naatsiilid (Sol 86, very fine-grained); 2) Pitted targets: Tselhbahih (Sol 51), Dahazkah (Sol 101; very fine-grained), Hedgehog (Sol 37: fine grained), Hastah\_tsaadah (Sol 87: mixed-sized: with phenocryst in a flowly, possibly glassy matrix), and Naakih\_tsaadah (Sol 110, medium grained with mesh-like pits); 3) Non-pitted targets: Dzilh (Sol 53, medium-grained), Hoolhnili (Sol 86, fine-grained), Dabikooh (Sol 101, medium-grained), and Ad\_ilidi (Sol 107, coarse-grained).

All textures are described in Table S3, including crumbly weathered surfaces (e.g., Nataani, Sol 75) and targets with uncertain textural assignments.

Rocks with clotted/coated textures have fine-grained (<1 mm), sometimes lustrous purple coatings, with fine-grained and homogeneous texture. Typical coated/clotted textures are represented by Tselhchee (Sol 15) and Naatsiilid (Sol 86) (see Figure 2). The example target Máaz (Sol 11–12) displays a clotted microtexture without apparent crystals and contains small (i.e.,  $\leq 500 \mu\text{m}$ ), rounded grains (described as “black-eyed peas”) that could be either embedded grains of regolith or formed through diagenetic processes. Some of these rocks with coated texture have a purple coating. We interpret these textures as resulting from alteration/secondary processes (Garczynski et al., 2022). Their compositions likely do not represent primary igneous compositions and thus are not used in calculations described in Sections 3.3 and 3.4 (Table S1).

We observed rock textures through RMI images suggesting very-fine grained ( $> 500 \mu\text{m}$ ), fine grained (0.5–1 mm), and mixed grain size textures (resembling porphyritic igneous texture) sometimes in a possibly vitreous matrix (see Figure 2). The very fine-grained and fine-grained textures are reminiscent of igneous aphanitic textures (described as such in Figures 3, 9–12). Unambiguous glass detection by the SuperCam instrument could not be performed directly. However, conchoidal fractures and shiny luster observed in some targets are consistent with either glassy material, or alternatively, wind polishing (e.g., Tselhbahih—Sol 51, Figure 2).

We also observed rocks with medium-grained (1–2 mm) and coarse-grained ( $> 2 \text{ mm}$ ) textures in the Máaz fm, as seen in targets such as Dabikoooh (Sol 101) and Ad\_ilidi (Sol 107; Figure 2), respectively. These textures, especially for coarse-grained textures, are reminiscent of igneous phaneritic textures (described as such in Figures 3, 9–12). Coarser-grained textures were observed in both pitted and non-pitted targets.

Both pitted and non-pitted fine-grained rocks were observed in the upper Máaz mb. Pitted rocks show different pit morphologies (spherical, hybrid, elongated, rounded, angular) (Table S3). In the upper Máaz mb, non-pitted textures are observed, including rocks like Dzilh (Sols 53 and 57) and Hoolhnili (Sol 86; Figure 2). Some non-pitted rocks (e.g., Dzilh, Bidziil, Hadahastsaa) display linear features and/or stretched grains. Unlike the lower Máaz mb, the Content mb only includes pitted textures (e.g., Content, Sol 239).

Abraded rocks were also imaged by RMI, namely on the targets Guillaumes (Sols 162–168), Bellegarde (Sols 187–191) and Alfalfa (Sols 371–378) (Figure S1 in Supporting Information S1). All abraded rocks display a micro-gabbroic texture with interlocking darker minerals, identified as pyroxene by the PIXL instrument (Planetary Instrument for X-ray Lithochemistry; micro-XRF—X-ray fluorescence—instrument located on the arm of the rover; see Allwood et al., 2020; Schmidt et al., 2022), and possible interstitial feldspar. Of note, Guillaumes exhibits pits (Figure S1 in Supporting Information S1), but their origin (primary or secondary) remains unclear.

To summarize, the different members of the Máaz fm and Content mb display varied and complex textures. Only the upper Máaz rocks have both pitted and non-pitted rocks. However, the lower Máaz mb lacks pitted rocks and therefore, shows less diversity in texture than upper Máaz rocks. Conversely, all the rocks observed in the Content mb have a pitted texture, which could possibly be due to a bias in sampling, as we investigated a limited region of this member.

### 3.3. Chemistry of Máaz fm and Content mb Rocks

Here we investigate here the chemistry of the Máaz fm, split into lower, upper, and Roubion mbs, and the Content mb (Figure 3). For each selected textural group (see Section 3.2), we average all the LIBS points that represent the primary igneous textures on non-abraded surfaces (see Section 2), and fitting criteria described in Section 2. Due to the fact that the upper Máaz mb shows more textural diversity, we group according to grain-size: with fine-grained (<1 mm; 48 LIBS analyses) and coarser-grained textures ( $> 1 \text{ mm}$ ; 128 LIBS analyses), whereas we averaged all textures for the lower Máaz mb (59 LIBS analyses) and Content mb (47 LIBS analyses). For all the members, we do not observe correlations between distance from target and bulk compositions (Table 1). No evident correlation exists between compositions and the primary textures in each of the three members. The mixed texture (including Hastah\_tsaadah and Alk\_es\_disi, Figure 2) stands out with lower  $\text{SiO}_2$  (46.6 wt.%) and higher FeO (25.3 wt.%), likely due to the presence of Fe-Ti-oxides (as single mineral or in mixtures in several LIBS point analyses).

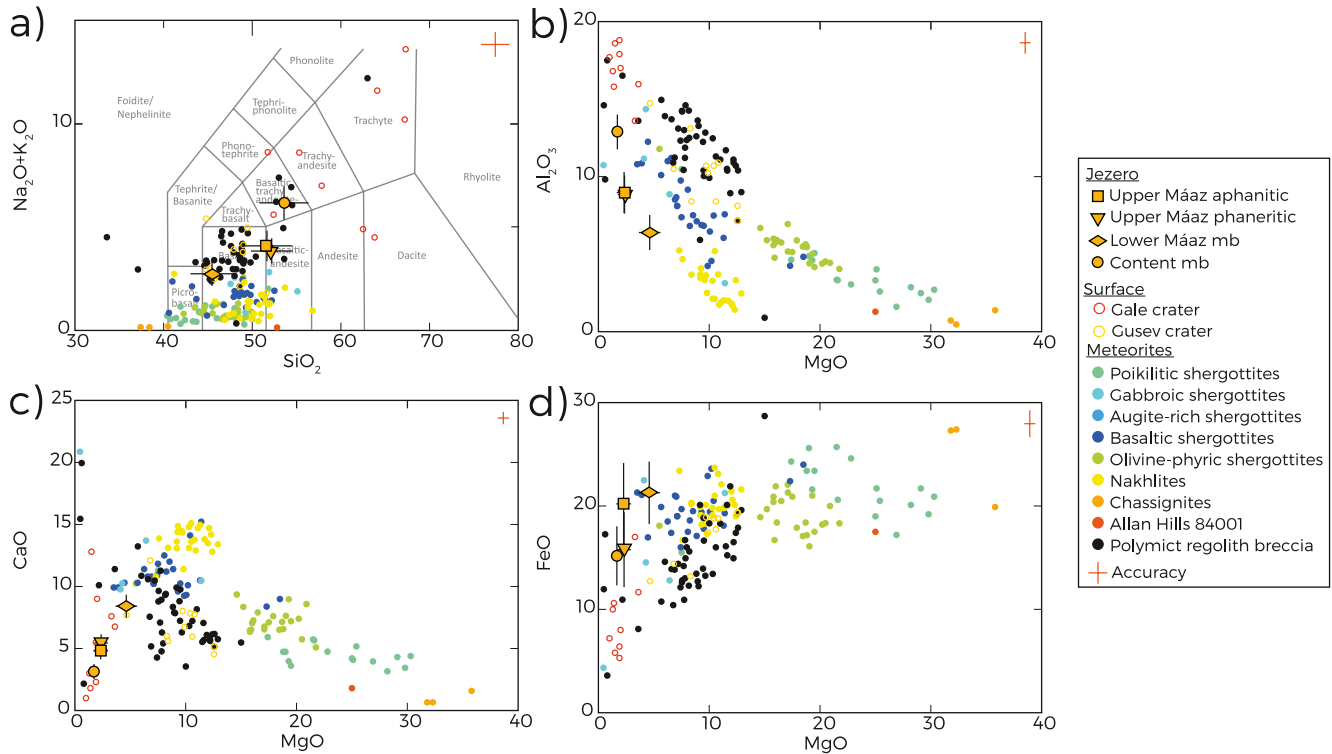


**Figure 3.** Major element compositions for the upper and lower Mááz mb and Content mb: (a)  $\text{Na}_2\text{O} + \text{K}_2\text{O}$  versus  $\text{SiO}_2$ , (b)  $\text{Al}_2\text{O}_3$ , (c)  $\text{CaO}$ , (d)  $\text{FeO}$  versus  $\text{MgO}$ , in comparison with Martian meteorite compositions, and Gale and Gusev crater compositions (see Text S1 in Supporting Information S1 for references). Error bars represent 1 standard deviation. Accuracy from Anderson et al. (2022) represented in orange. The Mááz mb and Content mb compositions are slightly enriched in alkali elements and depleted in  $\text{MgO}$  compared to Martian meteorites.

We compare the different major element compositions of the various textural groups within the three members (Table 1, Figure 3). The Mááz formation rocks range from basaltic to basaltic-trachy-andesitic (Figure 3a). The fine-grained rocks in the upper Mááz mb show a very similar composition to upper Mááz coarser-grained rocks, with 52 wt.%  $\text{SiO}_2$ , 9 wt.%  $\text{Al}_2\text{O}_3$ , 16–20 wt.%  $\text{FeO}$ , and  $\text{Mg}\#$  of 17–21 (all represent average compositions). For all groups, fine-grained and coarser-grained rocks display nearly identical compositions (Table 1). The Content mb also shows very similar composition to the upper Mááz mb with 53 wt.%  $\text{SiO}_2$ , 15 wt.%  $\text{FeO}$ , (the lowest  $\text{FeO}$  in the Mááz fm), and  $\text{Mg}\#$  of 17, but with higher  $\text{Al}_2\text{O}_3$  (13 wt.%) and total alkalis ( $\text{Na}_2\text{O} + \text{K}_2\text{O} = 6.1$  wt.%). The fine-grained rocks in the lower Mááz mb are more primitive than the upper Mááz mb with lower abundances of  $\text{SiO}_2$  (average of 45.3 wt.%) and  $\text{Al}_2\text{O}_3$  (6.4 wt.%), higher  $\text{MgO}$  (4.6 wt.%) and  $\text{Mg}\#$  of 28.

In addition to the chemical relationship of the different textures in the Mááz fm (Figure 3), we investigate the chemical relationships between the Mááz members defined in Horgan et al. (2022) and Crumpler et al. (2023) (Figure 4). Note that Content average composition in Figure 3 (aiming at a textural analysis) was derived from LIBS data collected on rocks with primary igneous textures only. By contrast, the Content composition average in Figure 4 was derived from all the rocks classified in Content mb using Mastcam-Z, for example, also including a coated texture (Figure 4). Artuby, Rochette, and Roubion mb (lower Mááz mb) have largely the same compositions (46–49 wt.%  $\text{SiO}_2$ , 7–9 wt.%  $\text{Al}_2\text{O}_3$ , 20–22 wt.%  $\text{FeO}$ ), with Artuby showing a  $\text{MgO}$  content higher than the two other members (8 wt.% vs. 3 wt.%) and could be part of the same group as proposed by Wiens et al. (2022) and Horgan et al. (2022). Nataani and Ch'ail (upper Mááz mb) in addition to the Content mb (52–53 wt.%  $\text{SiO}_2$ , 17–18 wt.%  $\text{FeO}$  for all three mbs) also show very similar compositions, with slightly higher silica and alkali contents than the Artuby/Rochette and Roubion mbs.

The clustering from our PCA analyses using the different major elements as variables (see Section 2.3; Figure 5) shows that targets belonging to the Mááz mb do not show differentiated clustering, and they appear all together in a rather heterogeneous group. PC1 indicates that the upper Mááz samples have higher silica and alkali element abundances than others. The samples belonging to the lower Mááz mb do not form a cluster clearly differentiated

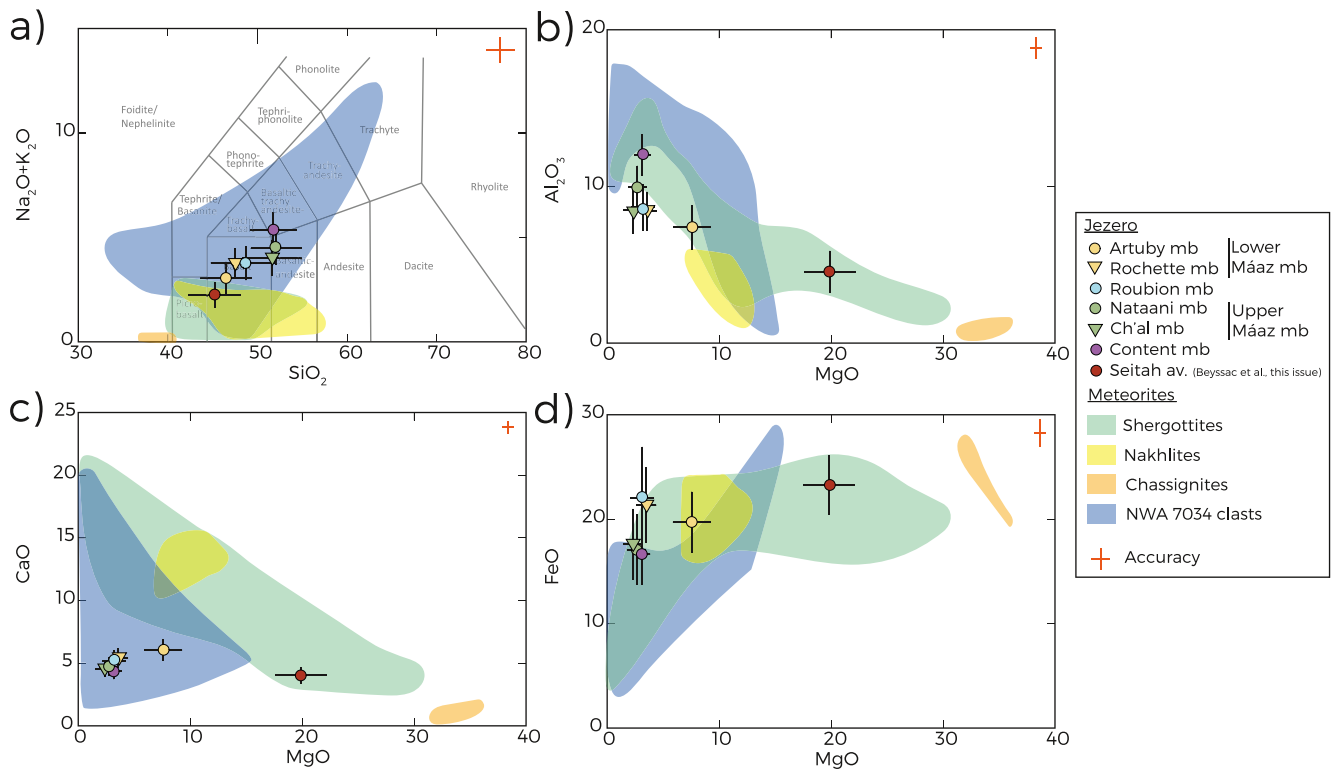


**Figure 4.** Major element compositions of textural groups defined by Horgan et al. (2023): (a)  $\text{Na}_2\text{O} + \text{K}_2\text{O}$  versus  $\text{SiO}_2$ , (b)  $\text{Al}_2\text{O}_3$ , (c)  $\text{CaO}$ , (d)  $\text{FeO}$  versus  $\text{MgO}$ , with Martian meteorite compositions, and Gale and Gusev crater composition envelopes (see Text S1 in Supporting Information S1 for references). Error bars represent 1 standard deviation average. Accuracy from Andersen et al. (2021) represented in orange. The different members included in the lower and upper Mááz members are very similar, with Artuby being more enriched in  $\text{MgO}$ . The Content mb shows similar compositions to the upper Mááz mb.

from upper Mááz, but do show a higher content in  $\text{CaO}$  and/or  $\text{TiO}_2$ . Regarding Content mb samples, they appear together in the center of the Mááz cluster, with the exception of Rent and Chamatte (both less primitive than the other samples).

### 3.4. Mineralogies of Mááz and Content Rocks

Determining mineralogy from LIBS analyses can be done via CIPW norms,  $\text{Al}/\text{Si}$  versus  $(\text{Mg} + \text{Fe})/\text{Si}$ , and stoichiometric analyses. We focus here on primary igneous mineralogy.

We calculate the CIPW normative modal abundances of each member (Table 3 using the Hollocher, 2004, CIPW calculations). The upper Mááz rocks show 43% feldspar, Content mb targets, being more enriched in  $\text{Al}_2\text{O}_3$ , contain 62% feldspar, whereas the lower Mááz mb contains 31% feldspar. The pyroxene abundance in rocks from the Content mb reaches 29%, while it reaches 39%–43% and 61% in rocks from the upper and lower Mááz mbs, respectively, with similar results obtained by Wiens et al. (2022). Normative hypersthene (Ca-poor orthopyroxene) is more enriched than diopside (Ca-rich clinopyroxene) in upper Mááz mb and Content mb, whereas the opposite is true for the lower Mááz mb. The quartz normative modal abundances vary from 0% (lower Mááz mb) to 13% (upper Mááz mb fine-grained).

Plotting the rocks in a molar  $\text{Al}/\text{Si}$  versus (vs.)  $(\text{Mg} + \text{Fe})/\text{Si}$  diagram allows the examination of their specific mineralogical composition as well (Figure 6). Mineral endmembers shown on Figure 6 correspond to SCCT measurements performed while *Perseverance* was exploring the Mááz fm (Cousin et al., 2022; see Table S1 for SCCT compositions). Rocks with very fine-grained and mixed-sized textures show a more restricted compositional range, likely representing mixtures within the probed areas and the potential presence of glass or a fine-grained groundmass, whereas coarser-grained textures show a trend between andesine, diopside and orthopyroxene. Rocks from the lower Mááz mb have more Mg- and Fe-rich compositions and are more concentrated around the diopside and orthopyroxene endmembers and appear to include less feldspar than the upper Mááz rocks.

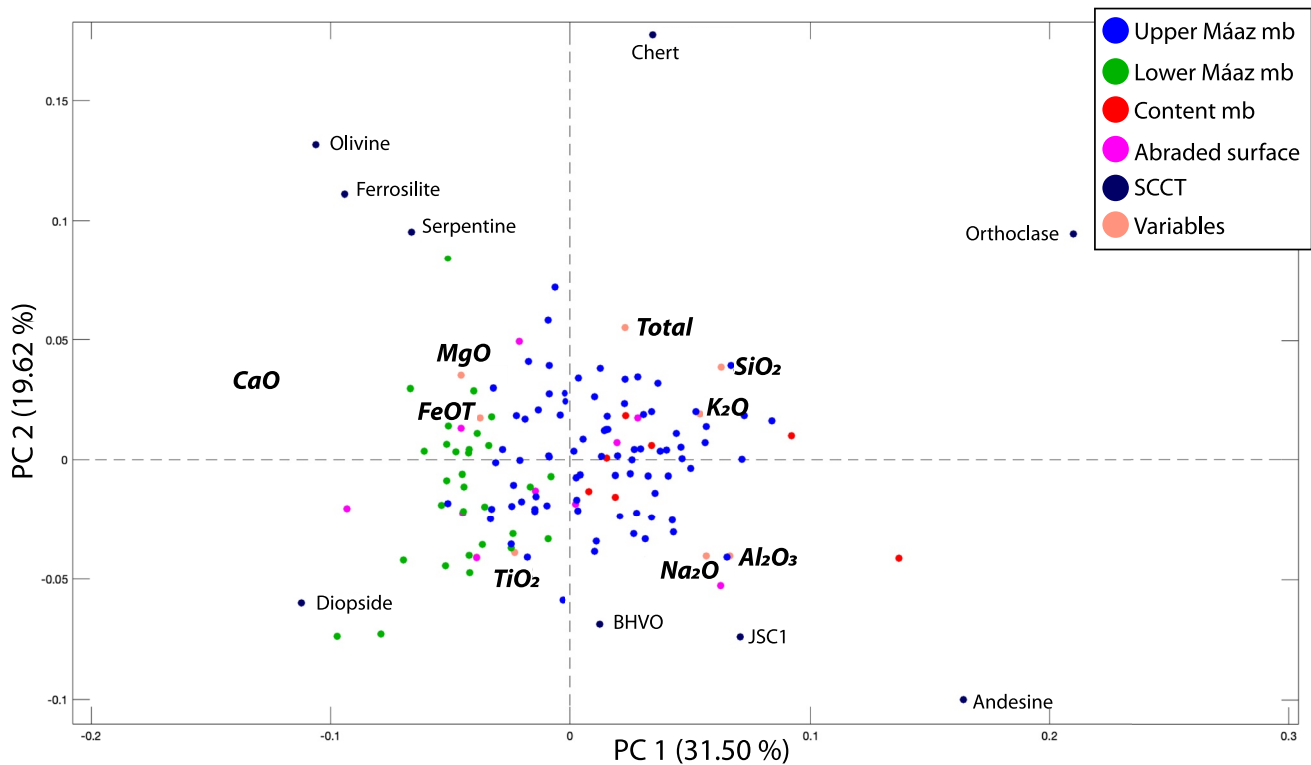


**Figure 5.** Projection of the scores and loadings (biplots) on PC1 and PC2 obtained after PC analysis (PCA) with the 8 different LIBS oxides and totals as scores (samples). Dark blue circle represent nine SCCT (Cousin et al., 2022) and the loadings (i.e., variables), here the oxides, are indicated in salmon pink. The Content mb overlaps the upper Máaz mb and the lower Máaz mb are more primitive than the two other mbs.

Conversely, the Content mb rocks have higher silica and alkali element abundances with compositions falling on the orthoclase-diopside trend, suggesting a more alkaline composition.

The LIBS laser beam is small enough to hit single phases in some cases. Single primary minerals were identified based on their stoichiometric characteristics similar to the pyroxene, plagioclase, and olivine SCCT measured on Mars (Table S4 for stoichiometric characteristics; see Cousin et al., 2022, for the compositions of SCCTs). Both MOC data (average for each observation point within a target) and shot-to-shot data (based on a spectrum from

each of the 30 laser shots within a given observation point) were considered to determine the single mineral compositions. For the shot-to-shot data, we ignored the first five shots that are dominated by surface dust and verified that, for a given point, most of the shots had the correct stoichiometry for the inferred single mineral phase.

We identified 20 single pyroxene grains in the Máaz and Content mb, including augite grains ( $Wo_{30-50}En_{10-22}Fs_{29-55}$ ) and Fe-rich low-Ca (pigeonite to ferrosilite) pyroxene grains ( $Wo_{3-9}En_{4-18}Fs_{73-93}$ ), that form a trend from the augite-rich endmember to the Fs (ferrosilite) -rich endmember (Figure 7, Table S5). Among these 20 single pyroxenes, one was observed in a target from the Content mb. Note that the pyroxene grains are not distinguishable on the RMI images. No specific composition can be related to a given member: the trend shown in Figure 7 is defined by pyroxenes found in both the upper and lower Máaz mbs and in the Content mb. Single pyroxenes were also shot in the abraded rocks: Guillaumes contains a Fe-rich, low-Ca pyroxene ( $Wo_3En_5Fs_{92}$ ) and a Fe-rich augite ( $Wo_{29}En_{15}Fs_{56}$ ), Bellegarde contains an augite ( $Wo_{38}En_{16}Fs_{46}$ ), and Alfalfa contains a Fe-rich pyroxene ( $Wo_7En_3Fs_{90}$ ). Of note, clinopyroxene was the only igneous (i.e., primary)

**Table 3**  
CIPW Normative Modal Abundances of the Different Máaz Members

| wt. %       | Upper Máaz fine-grained | Upper Máaz coarser-grained | Lower Máaz | Content mb |
|-------------|-------------------------|----------------------------|------------|------------|
| Quartz      | 12.7                    | 7.72                       | 0.00       | 4.09       |
| Feldspar    | 42.7                    | 42.7                       | 31.1       | 62.0       |
| Plagioclase | 35.0                    | 35.4                       | 28.6       | 50.3       |
| Orthoclase  | 7.74                    | 7.33                       | 2.54       | 11.7       |
| Pyroxene    | 38.5                    | 43.3                       | 61.3       | 29.0       |
| Diopside    | 17.6                    | 14.8                       | 34.0       | 4.79       |
| Hypersthene | 20.9                    | 28.5                       | 27.3       | 24.2       |
| Ilmenite    | 1.84                    | 1.08                       | 1.73       | 1.04       |
| Magnetite   | 4.25                    | 5.25                       | 5.70       | 3.91       |
| Total       | 100.0                   | 100.0                      | 100.0      | 100        |

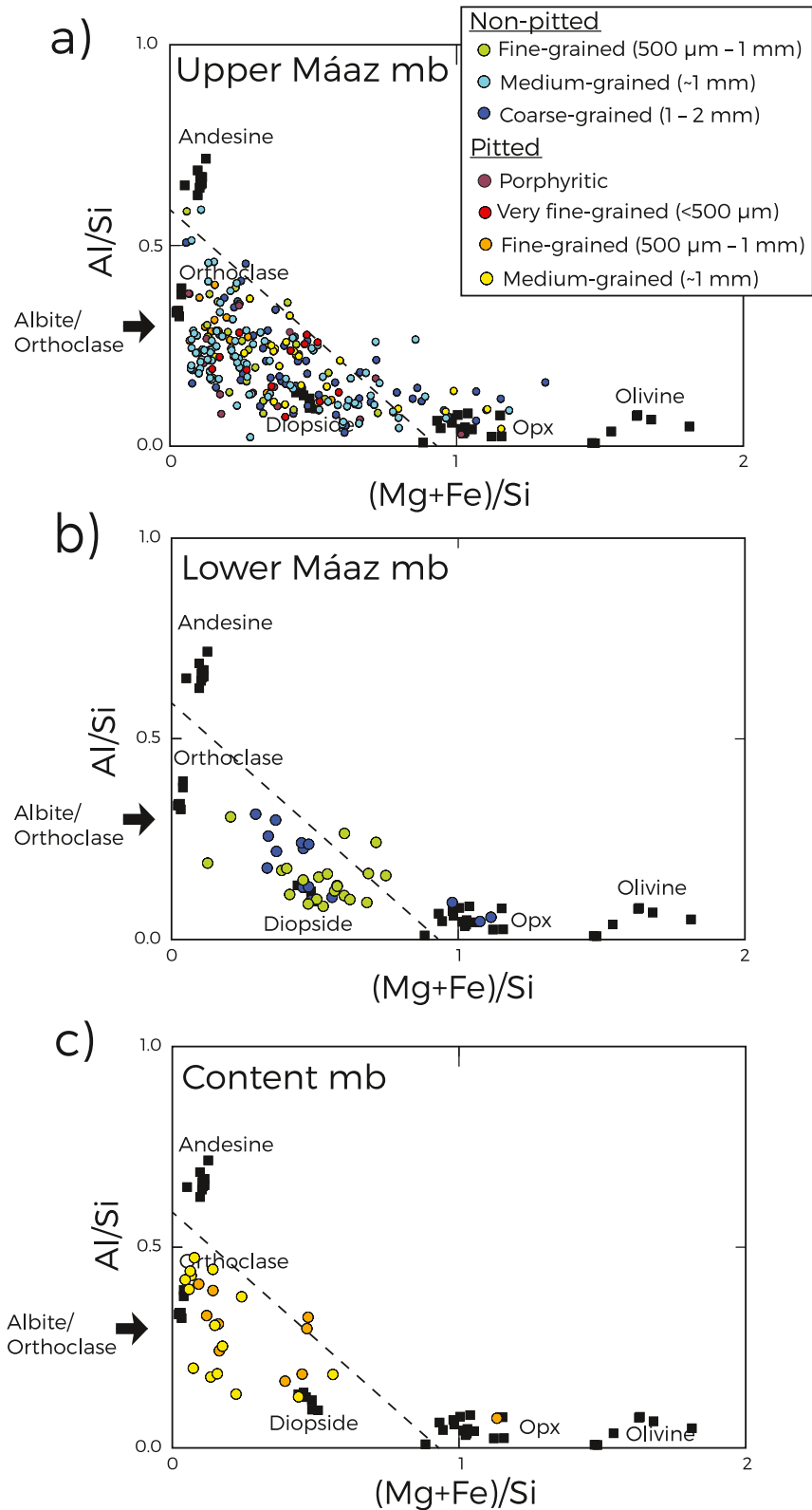


**Figure 6.** Molar Al/Si versus (Mg + Fe)/Si diagram for (a) Upper Máaz mb, (b) Lower Máaz mb, and (c) Content mb. The black squares are endmembers, corresponding to SCCTs analyzed in the Máaz formation (from Cousin et al., 2022). The upper Máaz mb shows compositions forming a trend between andesine and Opx endmembers (Opx = orthopyroxene), indicated by the dashed tie-line. Stoichiometric albite/orthoclase is shown by an arrow. The lower Máaz mb compositions are more concentrated around diopside and opx endmembers. The Content mb compositions are closer to the orthoclase endmember.

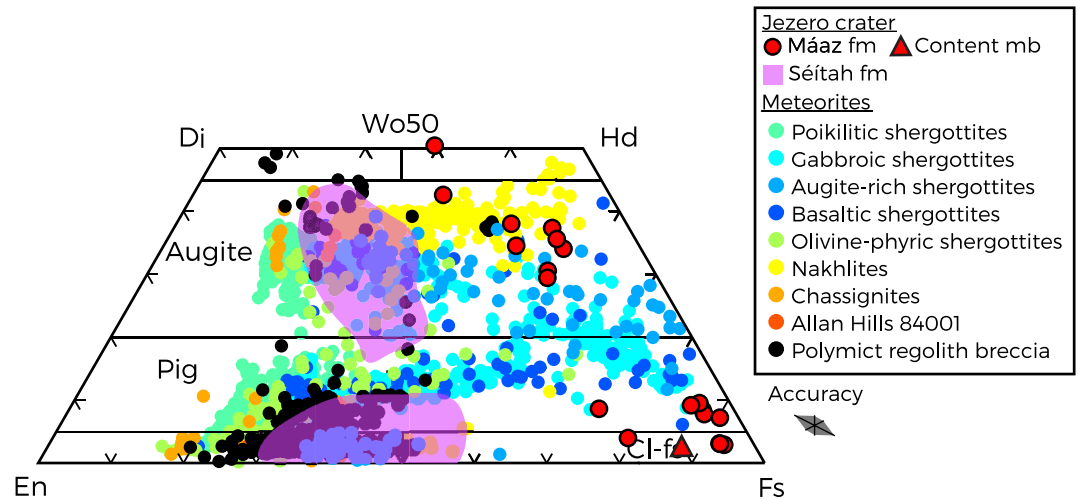


**Figure 7.** Pyroxene quadrilateral including stoichiometric pyroxene from the Mááz fm and Content mb and from the Séítah fm (Beysnac et al., 2023; see Text S1 in Supporting Information S1 for references). Accuracy is indicated as a dark gray diamond. The Mááz and Content pyroxenes show a Fe-rich trend between augite and Fs compositions and have different compositions than the Séítah pyroxenes.

mineral detected by VISIR, including both non-abraded surfaces and abraded patches in the Mááz fm (Mandon et al., 2022; Mandon et al., 2023).

One single plagioclase grain was analyzed, located in the Content mb in the Amignon target (Sol 246) with a composition of  $Ab_{66}An_{28}Or_6$  (Figure 8). Since plagioclase is likely ubiquitous in rocks from the Mááz fm given their basaltic or basaltic-andesitic compositions, the detection of only one single plagioclase suggests plagioclase grains are very small in these rocks. Most of our LIBS (and a few Raman) observations including plagioclase involve mineral mixtures. For example, points such as point #2 in the Alfalfa target (Sol 371) and point #7 in the Montpezat target (Sol 350) appear to contain a large proportion of plagioclase. No single olivine was detected, either by LIBS or VISIR (Mandon et al., 2022; Mandon et al., 2023).

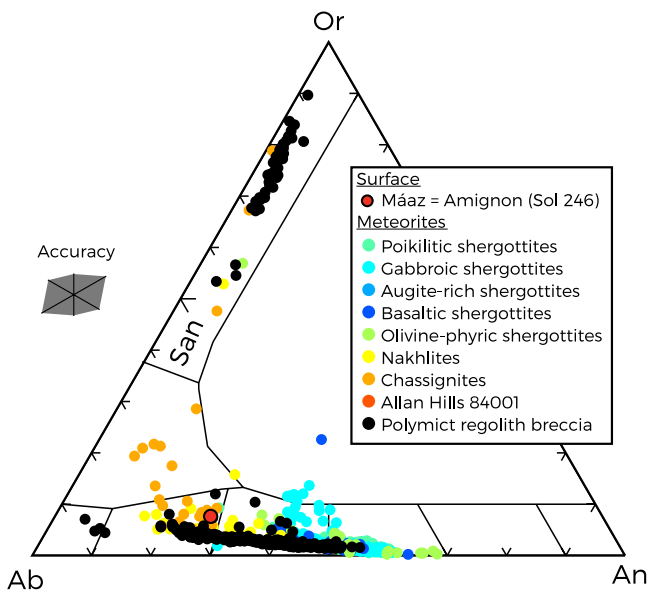


**Figure 8.** Feldspar ternary diagram including stoichiometric plagioclase from the Content mb (see Text S1 in Supporting Information S1 for references). Accuracy is defined by the dark gray diamond. Only one single plagioclase was found, see text for details.

A few other minor minerals were detected using LIBS data simply based on the MOC compositions (Table S5). Some Si-rich points (>70 wt.%  $SiO_2$ ), possibly consisting of Si-rich glass, were found in the Foux (Sol 138, point #2) and Beaujeu\_scam (Sol 140, point #8) targets. They possibly consist of Si-rich glass, their silica contents (up to 82 wt.%) being too low for a pure silica phase. We analyzed four potential Fe-oxide grains (see Table S5) all found in the Rochette mb, based on FeO content from 81 wt.% to 83 wt.% and a very low  $SiO_2$  content (1–6 wt.%). They possibly correspond to ferrihydrite as seen in IR spectra (Mandon et al., 2022; Mandon et al., 2023). No Cr-rich phases were encountered in the Mááz fm in contrast to what was found in the Séítah fm (Beysnac et al., 2023). Phosphate (likely apatite) was possibly detected in Alk\_es\_Disi (Sol 91) and the Guillaumes and Bellegarde targets, based on their phosphorus and CaCl-content using LIBS spectra, but was not confirmed by Raman and TLR analyses, reflecting a likely too small of a grain size for the large Raman analytical footprint.

### 3.5. Thermodynamic Modeling

To investigate the petrogenetic link between the upper and lower Mááz mb and the Content mb, we conducted MELTS modeling as described in Section 2.2. Model results at different pressures are largely similar. At near-surficial pressures (1 atm), initial water contents also play an insignificant role in mineral stability and liquid line of descent (compositional evolution in the liquid) as

water begins exsolving at the onset of every model. At 1 kbar, 1.0 wt.% initial H<sub>2</sub>O line of descent compositions for all are slightly more alkaline. We focus here on results for 1 atm (near-surface conditions) models with initial 0.07 wt.% H<sub>2</sub>O (= dry conditions, as we cannot constrain water content). We include the liquid lines of descent for all starting compositions in Figure 9. Here we aim to demonstrate that the liquid lines of descent overlap, representing a possible petrogenetic link.

### 3.5.1. Silicate Melt Chemistry

Lower Máaz mb evolutionary trends are the most primitive overall when compared to other members, with SiO<sub>2</sub> contents ranging from 50.4 wt.% to 80.1 wt.%, and MgO ranging from 0.0 wt.% to 5.1 wt.% (Figure 9a). The lower Máaz model has the sharpest FeO<sub>T</sub> depletion, which together increase from 23.9 wt.% to 26.4 wt.% until 1090°C, after which additional fractionating plagioclase and increasingly ferroan pyroxene deplete the liquid in FeO<sub>T</sub> to 1.3 wt.% (Figure 9e). Unlike the models with other starting compositions, lower Máaz model is steadily depleted in CaO by pyroxene and plagioclase, from 9.4 to 0.9 wt.% (Figure 9b).

Overall, both coarser-grained and fine-grained upper Máaz models show very similar liquid lines of descent for all oxides. SiO<sub>2</sub> enrichment (55.6–74.9 wt.% and 58.2–80.3 wt.% respectively) and coupled CaO and Al<sub>2</sub>O<sub>3</sub> depletion begin after the onset of plagioclase formation (Figures 9a–9c). In contrast, Al<sub>2</sub>O<sub>3</sub> depletion occurs while CaO is relatively enriched (2.2–2.5 wt.%) in the Content mb models after pigeonite formation begins, following prolonged plagioclase formation (Figure 9b). Alkalis Na<sub>2</sub>O and K<sub>2</sub>O are relatively enriched in all models, first gradually until the onset of pyroxene crystallization, and then more rapidly (Figures 9d and 9f). Potassium is depleted in all models in late stages when potassium feldspar crystallizes. This effect is most apparent in the Content mb model, where K<sub>2</sub>O drops from 5.0 to 3.6 wt.%.

The models from different starting compositions are fairly similar to one another, and tend to converge and display parallel trends, with a few exceptions. The Content mb is the most alkali- and alumina-enriched, and evolves to become increasingly siliceous from the basaltic-trachyandesite field, when plotted for its total alkali and silica content (Figure 9g). Models for the two upper Máaz members follow a similar evolutionary trend from the basalt/basaltic andesite fields, while lower Máaz follows the same trend from a magnesian basalt (Figure 9g).

### 3.5.2. Mineralogy

All models generate the same minerals including pyroxene (both augite and pigeonite), plagioclase, and spinel (magnetite to ulvöspinel), with minor amounts of tridymite (i.e., SiO<sub>2</sub>-phase) and potassium feldspar. Augite is the liquidus phase (first phase to crystallize) for the lower Máaz member (at 1150°C), while pigeonite is the liquidus phase for both of the upper Máaz members (at 1110°C for both textural members) (Figure 10). Plagioclase is the liquidus phase for the Content member due to the relative Al<sub>2</sub>O<sub>3</sub> enrichment of this member (Figure 10).

Pigeonite in all models span a similar range of MgO and FeO. Content models are the most CaO-depleted (En<sub>19–32</sub>Fs<sub>63–75</sub>Wo<sub>4–8</sub>), followed by coarser-grained upper Máaz mb (En<sub>19–34</sub>Fs<sub>61–69</sub>Wo<sub>6–12</sub>), fine-grained upper Máaz mb (En<sub>21–36</sub>Fs<sub>56–62</sub>Wo<sub>7–13</sub>) and lower Máaz mb (En<sub>29–14</sub>Fs<sub>57–69</sub>Wo<sub>12–14</sub>) (Figure 11). The lower Máaz mb crystallizes the most magnesian augite (En<sub>0–64</sub>Fs<sub>0–64</sub>Wo<sub>12–14</sub>). The upper Máaz and the Content members crystallize near-endmember hedenbergite, crystallizing compositions of En<sub>0–23</sub>Fs<sub>44–64</sub>Wo<sub>34–44</sub> and En<sub>0–15</sub>Fs<sub>49–63</sub>Wo<sub>36–38</sub>, respectively (Figure 11). The measured single pyroxene compositions are more Fe-rich than those modeled (Figure 11); this is addressed in Section 4.1.

Lower Máaz mb models generate the most albitic compositions (Ab<sub>33–62</sub>An<sub>10–66</sub>Or<sub>1–28</sub>) for plagioclase (Figure 12). Otherwise, there is significant compositional overlap for plagioclase in models: Ab<sub>33–56</sub>An<sub>5–65</sub>Or<sub>2–58</sub> for coarser-grained upper Máaz mb, Ab<sub>31–54</sub>An<sub>4–67</sub>Or<sub>2–63</sub> for fine-grained upper Máaz mb, and Ab<sub>35–58</sub>An<sub>4–56</sub>Or<sub>3–61</sub> for Content. Potassium feldspar compositions show more variability between models, with fine-grained upper Máaz mb reaching endmember orthoclase (Ab<sub>0–31</sub>An<sub>0–2</sub>Or<sub>66–100</sub>). Lower Máaz feldspar spans Ab<sub>12–55</sub>An<sub>0–1</sub>Or<sub>43–87</sub>, while coarser-grained upper Máaz mb and Content mb produce similar compositions of Ab<sub>31–32</sub>An<sub>2</sub>Or<sub>66–67</sub> and Ab<sub>22–32</sub>An<sub>0–2</sub>Or<sub>66–78</sub>, respectively (Figure 12).

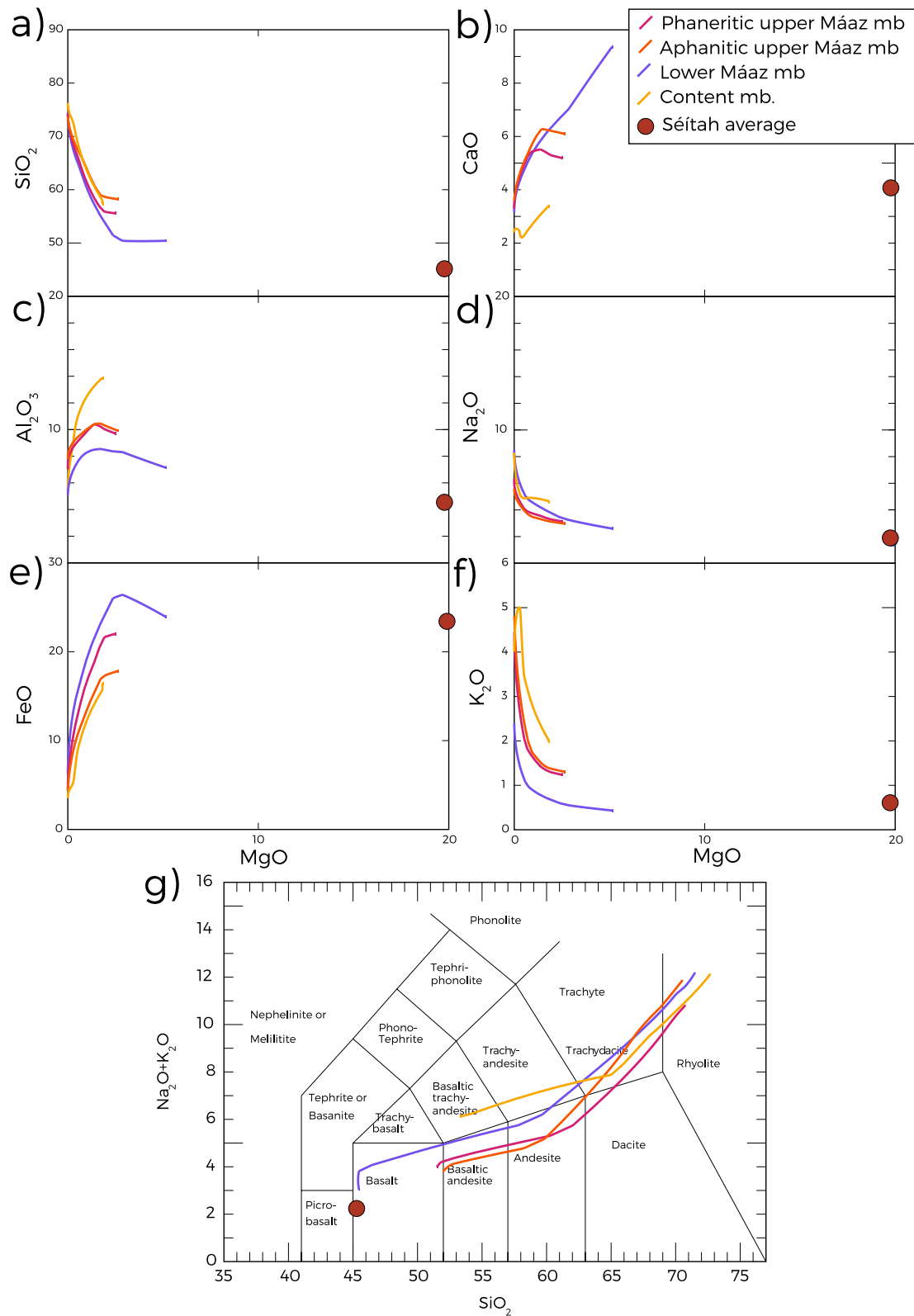


**Figure 9.** Major element diagram of modeled liquid lines of descent for the four starting compositions described in text, with (a)  $\text{SiO}_2$ , (b)  $\text{CaO}$ , (c)  $\text{Al}_2\text{O}_3$ , (d)  $\text{Na}_2\text{O}$ , (e)  $\text{FeO}$ , (f)  $\text{K}_2\text{O}$  vs.  $\text{MgO}$  and (g) TAS diagram. The average Séitah SuperCam LIBS analyses are from Beysac et al. (2023). All starting compositions have been normalized for totals equaling 100%. Note that the liquid lines of descent are very similar for the four starting compositions, with lower Máaz mb being slightly more primitive and Content mb enriched in  $\text{Al}_2\text{O}_3$  and depleted in  $\text{CaO}$  compared to the upper Máaz mb.

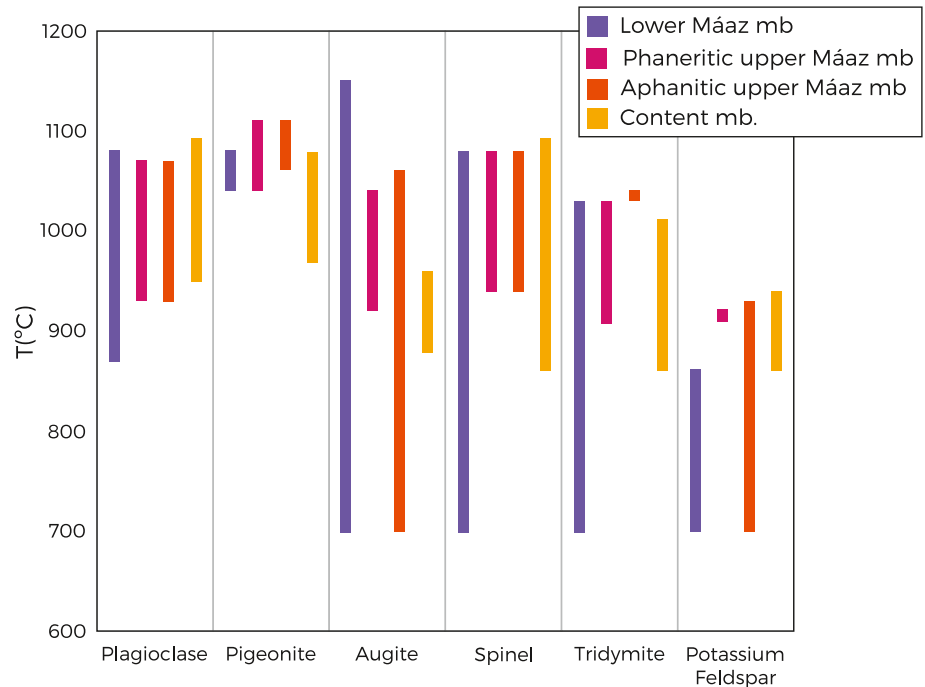


**Figure 10.** Crystallization sequence based on our model calculations using the Rhyolite-MELTS algorithm for fractional crystallization for all crystallized minerals. Both textures in upper Máaz mb have similar mineralogy with more augite crystallized for the fine-grained texture, similar to the lower Máaz mb. The Content mb crystallized more plagioclase and pigeonite compared to the Máaz fm.

## 4. Discussion

### 4.1. Máaz Formation as Potential Igneous Rocks

#### 4.1.1. Composition and Mineralogy

The Máaz fm, including the upper and lower Máaz mbs and the Content mb, have compositions ranging from basaltic—the main composition of the crust of Mars (McSween et al., 2009; Udry et al., 2020)—to basaltic-andesite and basaltic trachyandesite. The latter compositions are rarer on Mars, though present, for example, in rocks in Gale crater, and within Martian meteorites (Santos et al., 2015; Sautter et al., 2015).

As revealed by SuperCam measurements, the rocks from the Máaz fm and Content mb all contain pyroxene and (fine-grained) plagioclase as major phases, and minor oxides, a silica-rich phase, and other alteration minerals (see Clavé et al., 2022; Clavé et al., 2023; Mandon et al., 2022; Mandon et al., 2023). All of these minerals

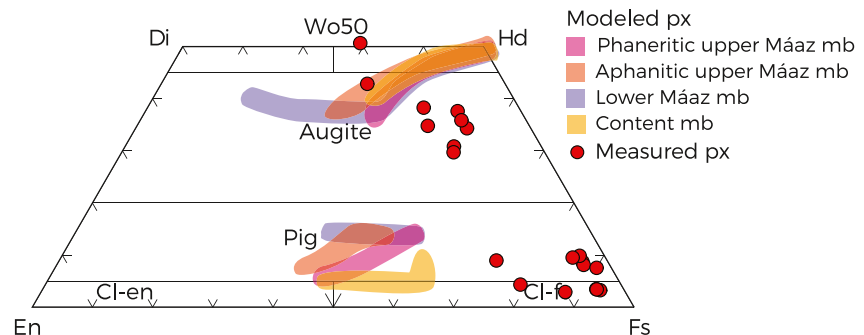


**Figure 11.** Modeled pyroxene compositions for the four starting compositions compared to our measured pyroxene compositions at 1 bar, FMQ and 0.07 wt.% H<sub>2</sub>O. All of our models produced two pyroxene populations: pigeonite and augite. However, the modeled pyroxene compositions are more Mg-rich than the measured Máaz pyroxenes.

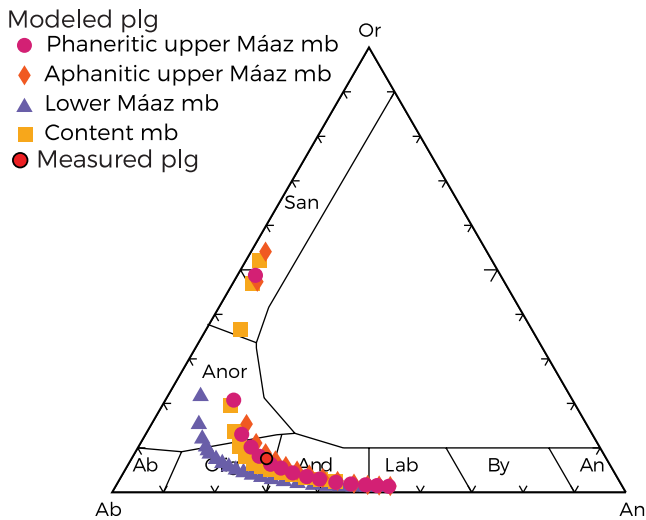


**Figure 12.** Modeled plagioclase compositions for the four starting compositions compared to our measured plagioclase compositions at 1 bar, FMQ and 0.07 wt.% H<sub>2</sub>O. All of our models produced similar plagioclase composition trends. The measured plagioclase belongs to the Content mb.

are commonly observed in terrestrial basalts and Martian meteorites (Udry et al., 2020). Olivine is also a common mineral in terrestrial and Martian meteoritic basalts, and has been identified in the Séítah fm (Beysac et al., 2023; Liu et al., 2022). However, SuperCam has not detected any olivine in the rocks of the Máaz fm.

The pyroxene grains have similar compositions in the various Máaz mbs and Content mb targets and follow a trend from Fe-rich augite to Fe-rich pigeonite, and possibly ferrosilite (Fs) (Figure 7). No trend with stratigraphy was observed in pyroxene compositions. Fe-rich augite and pigeonite coexist in several targets of similar Mg/Fe ratios (e.g., Guillaumes, Hastah\_tsaadah, and Mont\_Brune), indicating they are at equilibrium. The Fe-rich pyroxene compositions close to the Fs endmember compositions measured in the Máaz fm are rare on Earth and are formed either through: 1) high-pressure crystallization (Lindsley, 1983), or 2) breakdown of pyroxferroite or metastable pyroxene into hedenbergite + fayalite + quartz (=symplectite), the intimate mixture of the latter two manifest as ferrosilite within the laser spot size. Pyroxferroite, which is a metastable pyroxenoid at low pressures (Aramovich et al., 2002), has a stoichiometric composition identical to pyroxene. If the Máaz fm consists of lava flows, high pressure crystallization is not expected and thus it is possible that large symplectites are present in these rocks. If the Fs-rich measured compositions are part of the pyroxferroite/metastable pyroxene, it would indicate relatively fast

cooling to form metastable pyroxenes that are not stable at low pressure. Previous work on lunar basalts demonstrated that preservation of pyroxferroite requires cooling at a rate faster than the equivalent to holding the rock at above 990°C for longer than three days (Lindsley et al., 1972). Pyroxferroite/metastable pyroxene compositions are found in the gabbroic shergottite Northwest Africa (NWA) 7320 meteorite (Udry et al., 2017). The high Fe content in pyroxene might be due to LIBS MOC accuracy error: indeed, we observe a trend between SiO<sub>2</sub> and FeO versus totals (Figure S2 in Supporting Information S1), with an increase of SiO<sub>2</sub> and FeO with MOC totals for all measured pyroxenes, likely representing matrix effects. If the measured FeO content is too high, the true pyroxene compositions would still fall on the observed trend in the pyroxene quadrilateral (Figure 7). However, this accuracy issue cannot solely explain these Fe-rich pyroxene compositions. High-Fe content in pyroxene is consistent with the positions of pyroxene absorptions bands in both Mastcam-Z in situ and CRISM orbital spectral data of the Máaz fm (Horgan et al., 2022).

Although LIBS analyses inferred only one single grain of plagioclase, the basaltic composition (Figure 3) and textures (including for abraded patches, Figure S1 in Supporting Information S1) and CIPW norms and MELTS modeling suggest that plagioclase is present as a major phase in these rocks. However, these plagioclase grains are likely too small to be measured as a non-mixture by the SuperCam LIBS beam, which might be consistent with a rapid cooling of lava.

#### 4.1.2. Textures

Although we established that the Máaz fm and Content mb rocks have basaltic to basaltic-andesitic compositions and mineralogy, investigating textures is crucial determining the nature of rocks, that is, their igneous or sedimentary nature. Rocks of the Máaz fm and the Content mb display a large variety of primary textures as observed on non-abraded surfaces, including pitted and non-pitted rocks, mixed-sized texture (similar to porphyritic) in a glassy matrix, and various grain sizes from less than 500 μm up to 2 mm. This diversity of textures is common in terrestrial lava flows (Figure 2).

Various pitted textures are observed in Máaz rocks. Different origins of pits are possible: the first possibility is that they are vesicles (primary vugs), representing simple degassing vesicles and stretched vesicles, and thus indicating igneous processes. Primary vesicles are likely present in the example targets like Dahazkah (Sol 101: very fine-grained), Hedgehog (Sol 37: fine-grained), and Hastah\_tsaadah (Sol 87: mixed-grained texture) (Figure 2). The latter has a texture showing evidence of flow and large crystals, potentially of feldspar (although we were not able to measure their compositions). A second possibility is that the pits are such as crystal-ghosts, also called crystal molding (secondary pits; ripped off and/or dissolved; individuals and agglomerates). Crystal

molding is an alteration process and missing mineral components, which may affect the bulk rock composition, thus, we did not include rocks with secondary pits in our bulk compositions (e.g., Naakih\_tsaadah—Sol 110), as Naakih\_tsaadah and other targets (see Table S3) likely underwent crystal-molding processes, and show a mesh-like texture with pits of various sizes, some having angular crystal-like shapes. According to our investigations, it is likely that only pitted rocks representing crystal molding are present (e.g., Sauze, Sol 184) in the lower Máaz mb but it is not clear if vesicular rocks were observed. The pits in some targets (Dahazkah, Hedgehog, and Hastah\_tsaadah, see Figure 2) are likely vesicles, formed by gas bubbles in lava that were volatiles that previously dissolved in the magma (see also Crumpler et al., 2023, for outcrop images). On Earth, vesicular rocks produced during effusive volcanism commonly contain finer-grained textures and glass, although glass is not necessarily present. For igneous rocks, grain sizes are an indicator of various magmatic processes, including cooling rate. We suggest that the very fine-grained and fine-grained targets (both reminiscent of aphanitic igneous textures), and mixed-sized and vesicular targets found in the upper Máaz fm, as well as Content mb targets are igneous effusive rocks. Targets showing typical effusive textures are Hedgehog and Hastah\_tsaadah. Some non-pitted rocks (e.g., Dzilh, Bidziil, and Hadahastaa) display linear features and/or stretched grains, which we interpret as possible flow features. Putative pāhoehoe ropy textures, commonly observed in basaltic lavas on Earth, were also observed by Mastcam-Z in the long-distance target Taa\_tsaadah (Sol 110). Note that these rocks could also contain some impact-related textures, such as shattercones, as Taa\_tsaadah is located close to a crater. Alfalfa is coarser-grained, but does exhibit a finer-grained matrix and therefore could be interpreted as a quenched lava flow.

Coarser-grained textures (reminiscent of phaneritic igneous textures) could potentially represent intrusive magmatism, with crystallization at some depth beneath the surface of Mars (Figure S3 in Supporting Information S1). However, coarser-grained and fine-grained textures are not systemically spatially distributed throughout the Máaz fm, that is, coarser-grained rocks do not consistently underlie fine-grained rocks. These findings imply that rocks with a coarser-grained texture do not have an intrusive and plutonic origin. Coarser-grained targets likely had a different cooling history, such as having formed in the middle of a lava flow, where lava would have stayed hotter for longer periods of time and thus formed coarser grains. The diversity of textures observed in Máaz rocks is common for terrestrial lavas flows (Figure 2). Textures and compositions reveal that the Máaz fm and Content mb are formed from different lava flows overlying the Séítah fm.

#### 4.2. Petrogenetic Link Between the Different Máaz Members

Using the mineralogy and composition of the different members (Ch'ał, Nataani, Roubion, Artuby, Rochette, Content), below described as lower Máaz (Artuby, Rochette), upper Máaz, (Nataani, Ch'ał), Roubion, and Content, we can constrain their possible petrogenetic links as well as constrain their link with the Séítah formation. The bulk major element composition of both lower and upper Máaz, as well as Content, are very similar (Figure 3, Table 1) and these members all show the same mineralogy. In particular, the pyroxene trend observed (Figure 7) is similar for the three members. The Content mb overlies the Séítah fm (Núñez et al., 2022). However, in contrast to rocks from the Séítah fm, those from the Content mb do not contain olivine, and their VISIR signature is very similar to that of the rocks from the Máaz fm (see Figure 10 from Mandon et al., 2022; Mandon et al., 2023). The average Mg# of the Content mb is 17, whereas it is 60 for the Séítah fm of 60 (Beyssac et al., 2023). Content mb mineralogy is the same as the Máaz mb compositions, including pyroxene compositions (Figure 7, Table S5), as well as its bulk compositions, although the former is more alkaline (Table 4, Figure 5). The textures of the Content mb rocks also share many similarities with rocks of lower and upper Máaz, such as the presence of vesicular textures. Thus, the mineralogy and compositions as well as textures confirm that the Content mb is not part of the Séítah fm and is likely linked to the Máaz fm. However, the overall stratigraphy of this member and its relationship with the Séítah fm is not yet understood: *It is possible that Content mb (thus the Content lava flow) overlies the eroded surface of Seitah and was then itself eroded, since no significant in-place continuous outcrops have been observed.*

Similar to the Content mb, we assess the lower Máaz mb and compare it to the Séítah fm. The Séítah rocks show a composition of 45.3 wt.% SiO<sub>2</sub>, 4.4 wt.% of Al<sub>2</sub>O<sub>3</sub>, 23.5 wt.% of MgO (vs. 2.3 to 4.6 wt.% MgO for the Máaz mb) and Mg# of 60 (17–28 for Máaz mb), suggesting that the Séítah fm is considerably more primitive than the Máaz fm. The pyroxene compositions in the Séítah fm, obtained by Beyssac et al. (2023) using the same method as in this study, are different: the Séítah pyroxenes are lower in Fe and seem to show two distinct populations, one

**Table 4**  
*Possible Origin of the Máaz Formation and Content Member*

| Different origins            | Lava flow | Cumulate | Pyroclastic flows | Impact melt | Clastic sedimentary |
|------------------------------|-----------|----------|-------------------|-------------|---------------------|
| Textures                     | –         | –        | –                 | –           | –                   |
| Presence of vesicles         | X         | –        | X                 | –           | –                   |
| Jointing crystals            | X         | X        | –                 | X           | –                   |
| Laminations                  | X         | –        | X                 | –           | –                   |
| Basaltic composition         | X         | X        | X                 | X           | X                   |
| Primary mineralogy           | X         | X        | X                 | X           | X                   |
| Regional draping lithologies | –         | –        | X                 | –           | –                   |

augitic and one pigeonite/ferrosilite (Figure 7). Furthermore, starting at Sol 202, olivine is observed in the target Issole (also observed in Entreaux—Sol 173), whereas olivine is not present in any of the Máaz mbs. Olivine is indeed ubiquitous in the Séítah fm (Beyssac et al., 2023). Thus, we conclude that the lower Máaz mb does not belong to the Séítah fm.

The thermodynamic models (Figure 9) show that the liquid lines of descent are roughly parallel in the space of most oxides between the different Máaz and Content members within SuperCam error, particularly between the lower Máaz mb, and the fine-grained and coarser-grained upper Máaz starting compositions. The lower Máaz model is slightly more primitive, and does not always follow the same trend, but does converge on fine-grained and coarser-grained upper Máaz models as it becomes less MgO rich (i.e., as it evolves). The lower and upper Máaz mbs are therefore likely co-genetic/related lava flows or are one single flow, although the latter possibility is less likely, given the large range in cooling history, textures, and surface weathering observed throughout the Máaz fm. Lower Máaz and upper Máaz mb exposures represent the most primitive, and the least primitive of the sampled portions of the melt, respectively. The Content mb is slightly more alkali and alumina-enriched than the Máaz fm, and its slightly different liquid lines of descent may result from those small differences (Figures 3 and 9). However, the Content liquid line of descent is parallel to the other Máaz mb, potentially representing a slightly more differentiated magma from a similar magmatic system. According to its unclear stratigraphy, the Content mb may result from (a) a batch of lava distinct from Máaz, or (b) the same parental melt but that underwent more extensive differentiation compared to the later-formed overlying members. However, no relative timing can be constrained solely based on its composition.

For all the Máaz members, the modeled pyroxene compositions are less Fe-rich than the pyroxene grains measured by LIBS (Figure 11, Table S5). We propose that this discrepancy is due to the MELTS calibration: this calibration is based on a terrestrial and extraterrestrial compositional database, but does not yet include the Fe-rich compositions that have been observed on Mars (e.g., Balta & McSween, 2013; Collinet et al., 2021). However, all the members show very similar modeled pyroxene compositions, although the lower Máaz mb has pyroxene compositions higher in Mg, as expected based on its more primitive bulk composition. Our models do not yield any olivine, in accordance with the Máaz fm observations. Both modeled and observed Máaz pyroxene compositions and trends are dissimilar from those observed in the Séítah fm, further supporting the conclusion that the Máaz and Séítah formations are likely not petrogenetically linked. In a broader sense, the Máaz and Séítah formations likely did not form from the same magmatic systems and this, therefore, implies that the Máaz is not the volcanic equivalent of Séítah cumulates.

Further studies on returned samples should examine trace element and isotopic data in order to better characterize the source of Máaz as well as Séítah to test the petrogenetic linkages proposed here (see Simon et al., 2022; Simon et al., 2023).

#### 4.3. Comparison of Máaz fm Rocks With Martian Meteorites

Martian meteorites are the only samples that we currently possess from Mars: they are all igneous with predominantly basaltic compositions (Figure 3), except for the NWA 7034 and its paired meteorites, which represent a regolith polymict breccia with igneous, impact, and sedimentary clasts (e.g., Agee et al., 2013; Hewins et al., 2017; Humayun et al., 2013; McCubbin, Boyce, Szabó, et al., 2016; Udry, Balta, & McSween, 2014; Udry, Lunning,

et al., 2014, 2020; Wittmann et al., 2015). Although the Máaz lithologies generally show basaltic compositions, some differences exist compared to the Martian meteorites. The Máaz lithologies are more enriched in alkali elements than most Martian meteorites (Figure 3), displaying alkali element abundances similar as some igneous clasts in NWA 7034 and paired meteorites (Santos et al., 2015) as well as some proposed parental melts for the chassignite meteorites (Nekvasil et al., 2007, 2009). The Máaz fm and Content mb compositions and mineralogies resemble non-olivine bearing meteorites, which consist of ~46% of the total Martian meteorite collection (Udry et al., 2020). Among these meteorites are basaltic shergottites, with similar CaO and Al<sub>2</sub>O<sub>3</sub> contents, however the Máaz mb and Content mb have some of the lowest Mg# (17–28) compared to all Martian meteorites, with a Mg# of 23–25 for Los Angeles, Mg# of 25–27 for the augite-rich shergottites NWA 8159 and NWA 7635, and Mg# of 34 for NWA 7320 (Herd et al., 2017; Rubin et al., 2000; Tait & Day, 2018; Udry et al., 2017).

The pyroxene compositions in the Máaz fm resemble late-stage pyroxene analyzed in the gabbroic shergottite NWA 7320 (Udry et al., 2017), and the basaltic shergottite Los Angeles (Rubin et al., 2000; Figure 7). The Fe-rich clinoenstatite analyzed in the Máaz rocks could be pyroxferroite (or the symplectite breakdown products thereof). The only single plagioclase measured in the Máaz fm (in Amignon) is richer in Na (An<sub>28</sub>Ab<sub>66</sub>Or<sub>6</sub>) than the plagioclases in most shergottites, but this is not surprising given that Amignon is part of the alkali-rich Content mb (Figure 8).

The abraded patches, which all display interlocking igneous textures, allow direct textural comparison with Martian meteorites (Figure S1 in Supporting Information S1). Micro-gabbroic textures and basaltic mineralogy found in the Máaz lithologies are extremely common in basaltic or gabbroic Martian meteorite shergottites (Udry et al., 2020). However, none of the Martian meteorites recovered so far shows a vesicular texture resembling that of some of the rocks (from non-abraded surfaces) from the lower Máaz and Content mbs, likely due to shock collapse during the launch of the meteorite from Mars (Liu et al., 2018). Note that vesicles are found in the shock melt of the Tissint meteorite (Walton et al., 2014). This difference in texture, as well as differences in composition, are consistent with other observations that reflect fundamental differences between surface rocks of Mars and Martian meteorites, attributable to various factors including filtering due to the ejection mechanism (e.g., Udry et al., 2020; Walton et al., 2008). Thus, the igneous rocks in Jezero contribute to a more comprehensive view of Mars petrology relative to the Martian meteorites.

In summary, the rocks from the Máaz fm and Content mb have compositions and textures similar to non-olivine bearing basaltic and gabbroic shergottites, although the Máaz fm and Content mb are less primitive and richer in alkali elements. They also contain similar Fe-rich pyroxene compositions similar to those analyzed in the Fe-rich meteorites NWA 7320 and Los Angeles. The Máaz lithologies most closely resemble those of Fe-rich meteorites such as the basaltic shergottites Dhofar 378 (Dreibus et al., 2002), Los Angeles (Rubin et al., 2000), the gabbroic shergottite NWA 7320 (Udry et al., 2017), the augite rich NWA 8159 (Herd et al., 2017) and some clasts of NWA 7034 (Santos et al., 2015). However, note that these meteorites do not have a pitted/vesicular texture.

#### 4.4. Comparison of Máaz Formation With Gusev Crater and Gale Crater Igneous Rocks

The Mars Exploration Rover *Spirit* landed in Gusev crater in 2004. In contrast to the less primitive rocks found in the Máaz fm, the Adirondack class basalts are near-primary melts and are olivine-bearing (Filiberto & Dasgupta, 2011; McSween, Wyatt, et al., 2006; McSween et al., 2008)—rocks not found among the Máaz fm. However, *Spirit* also encountered more alkali-rich rocks among the Irvine class and the Wishstone class rocks analyzed in Gusev crater (Na<sub>2</sub>O + K<sub>2</sub>O = 3.33 and 6.01 wt.%, respectively; McSween, Ruff, et al., 2006; Usui et al., 2008), which are more evolved and more alkali-rich than the Adirondack class basalts. Even the Irvine and Wishstone class rocks are more primitive than rocks in the Máaz formation based on Mg#, which are higher in the Irvine and Wishstone class basalts (i.e., Mg# of 51–61; McSween, Ruff, et al., 2006).

The Mars Science Laboratory *Curiosity* rover landed in Gale crater in 2012 and encountered a variety of igneous float rocks and pebbles mostly until ~ Sol 800 (Cousin et al., 2017; Sautter et al., 2015). Igneous Máaz rocks appear more chemically homogeneous compared to Gale crater rocks, which range from basaltic and andesitic to trachytic (Cousin et al., 2017; Sautter et al., 2014, 2015). Máaz rocks also show similar CaO and Al<sub>2</sub>O<sub>3</sub> compositions to Gale crater rocks (Figure 3; Sautter et al., 2015). A noticeable difference between Gale crater and Máaz fm lithologies is that most igneous rocks in Gale crater are not in place, likely explaining the compositional diversity of Gale crater rocks: they were sourced from various regions upstream of

the Gale crater watershed. The igneous rocks of Gale crater are rich in feldspar, including coarse grains of plagioclase (e.g., Harrison: Cousin et al., 2017; Sautter et al., 2014, 2015), and micas (muscovite) in conglomerates (e.g., Goulburn and Link targets; Forni et al., 2015), while feldspar occurs as very small grains in rocks from the Mááz fm. Based on the high-alkali mineralogy and bulk compositions found in Gale crater, Treiman et al. (2016) concluded that the igneous Gale crater rocks have a K-rich source. Pyroxene compositions in Gale crater are more similar to the Séítah fm pyroxene than the ones found in the Mááz fm (Payré et al., 2020; Figure 7).

Although Mááz rocks are igneous rocks, their compositions and textures are different from other surface Martian igneous rocks, indicating unique magmatic histories. These Mááz rocks appear to be derived from a previously unsampled mantle source compared to surface rocks analyzed in the Gale crater.

#### 4.5. Comparison With PIXL Results for the Mááz fm

The PIXL instrument located on the robotic arm of *Perseverance* can map the elemental compositions of abraded rocks using micro-X-ray fluorescence (XRF) with  $\sim 120 \mu\text{m}$  resolution (Allwood et al., 2020). In the Mááz fm, the abraded rocks Guillaumes, Bellegarde, Montpezat, and Alfalfa were analyzed by PIXL (see Schmidt et al., 2022). Consistent with SuperCam results, PIXL results indicate that these rocks have basaltic and trachy-andesitic compositions, particularly rich in Fe, and contain plagioclase and pyroxene. The PIXL instrument observed a plagioclase composition in the Alfalfa target of  $\text{Ab}_{63}\text{An}_{33}\text{Or}_4$ , a composition very similar to the one observed in the Amignon target in the Content mb using LIBS. The main difference, when compared to SuperCam data, is that PIXL only observed augitic pyroxene and not pigeonite, although augitic pyroxene observed with both LIBS and PIXL have similar compositions. PIXL also detected possibly late-stage, altered fayalitic olivine, in the three targets, which was not directly detected with SuperCam LIBS, TRR, nor VISIR, likely due to the small amount and/or small grain sizes. Overall, SuperCam and PIXL found similar mineralogical compositions for the Mááz rocks, indicating that the three abraded targets are representative of the Mááz compositions. However, the full diversity of textures in the Mááz and Content mb may not be depicted in the abraded rocks.

#### 4.6. Formation Hypotheses for the Mááz fm and the Content mb

The SuperCam investigations conducted on rocks from the Mááz fm and the Content mb allow the elucidation of hypotheses regarding their formation. The three members investigated here (i.e., the upper and lower Mááz mbs and the Content mb) show very similar basaltic to basaltic andesitic compositions, with low MgO and high FeO contents. We confirm with chemistry that Mááz can be split into upper and lower groups of members consistent with morphology and spectral properties (Horgan et al., 2022). The lower Mááz mb includes the Artuby and Rochette mbs, and possibly the Roubion mb, as noted by Wiens et al. (2022), while the upper Mááz mb includes the Ch'ał and Nataani mb, on the basis of their compositions.

The discoveries of the Mááz fm and Content mb expand on the diversity of Martian magmatism, including both diversity in textures and compositions. The Mááz fm and Content mb rocks are some of the more Mg-poor igneous rocks that we have analyzed from Mars, potentially revealing a Mg-poor (or Fe-rich) source, or preserving evidence of processes that caused extensive differentiation.

We interpret the Mááz fm and Content mb lithologies to be lavas with complex textures and compositions similar to Fe-rich pyroxene-bearing meteorites. We here discuss several possible scenarios for their formation and emplacement at the Martian surface:

1. The Séítah fm, which has been interpreted as an olivine-rich cumulate, formed through accumulation and gravity settling at the bottom of a large but shallow magmatic chamber or sill, or possibly a thick lava flow. Rocks from this formation exhibit distinct mineral assemblages, including olivine, and two pyroxene populations richer in Mg relative to the Mááz pyroxene populations. The Séítah and the Mááz fms likely did not originate from the same parental magma nor the same magmatic system, according to our current results, and could not have been differentiated from a single melt. Thus, we exclude the possibility that Mááz lava flows originated from the same magmatic chamber, where the Séítah fm formed and accumulated. Moreover, the Mááz fm is not the volcanic equivalent of Séítah. This does not prevent these formations from having the same magmatic source (i.e., reservoir).

2. The Mááz parental magma, Fe-richer and more differentiated than the Séítah parental magma, erupted and formed several thick lava flows, as represented by the variety of textures, including coarser-grained (possibly phaneritic)—possibly formed from slower cooling in the center of the lava flow—in the Mááz fm. According to our thermodynamical models, and bulk and mineralogical compositions, the upper and lower Mááz mb (and possibly the members also defined in Horgan et al., 2022; and Crumpler et al., 2023) are petrogenetically related, representing several consecutive thick lava flows from the same parental melt that was replenished with possible different recharges, and may represent magmas at different stages of evolutionary trends. Some of these lavas might have been rapidly cooled, as indicated by the possible presence of pyroxferroite.
3. Following the erosion of the Séítah fm magmatic chamber or sill, the Content mb, overlying the Séítah fm (Núñez et al., 2022), erupted and crystallized on top of the Séítah fm. However, we do not know the relative timing of its eruption compared to the different Mááz mbs. This stratigraphy does not preclude the existence of a unique parental magma for both the Content mb and the Mááz fm, consistent with bulk compositions, mineralogies, and modeling results.
4. Another possibility is that Séítah was emplaced as a sill or a diapir under the Mááz mb. The Mááz fm has opposing 10° dip angles that could be due to slight uplift with the emplacement of Séítah (Beysac et al., 2023). No contact metamorphism has been observed to confirm this hypothesis, but a thermally affected margin may not be evident due to the fact that both magma compositions had similar temperatures. A chilled margin along the contact with Séítah and Content could exist, but was not observed/observable by *Perseverance*.

The Mááz and Séítah fms may be part of equivalent to regionally extensive units outside of Jezero: the pyroxene-bearing mafic cap and regional olivine/carbonate-bearing unit (Goudge et al., 2015; Horgan et al., 2020; Hundal et al., 2022). In orbital data, it was shown that the mafic cap drapes the olivine-rich unit, which itself drapes the underlying topography (e.g., Kremer et al., 2019; Mandon et al., 2020; Sun & Stack, 2020). This stratigraphy is not expected for low-viscosity basaltic flows, as lava should pond in lower topography (Mandon et al., 2020), so a leading hypothesis for the regional units in recent years has been a pyroclastic origin (Kremer et al., 2019; Ruff et al., 2022). Thus, according to our results, it is difficult to deduce one unique solution for the formation of the regional units as well as the Séítah fm, Mááz fm, and the Content mb. Here we describe other possibilities for the formation of these lithologies (also described in Table 4). Keeping this in mind, we discuss hereafter other possible scenarios of formation for the Mááz fm (Table 4; Figure 13).

#### 4.6.1. Pyroclastic Origin

An alternative explanation for the Séítah and the Mááz fm is their emplacement through the processes of explosive volcanism, namely by: pyroclastic fall, where particles are advected by the wind and settle from the atmosphere; or by pyroclastic density currents (PDCs), which are ground-hugging mixtures of hot gas, ash and rock, that tend to occur in dense (“flow”) or dilute (“surge”) end-member styles, or a mixture of the two (Dufek et al., 2015). Both pyroclastic fall (Kremer et al., 2019) and PDC processes (Mandon et al., 2020; Ruff et al., 2022) have been invoked to explain the regional olivine-bearing unit that Séítah is hypothesized to be related to, and pyroclastic fall has been suggested as an origin for the regional capping unit (Hundal et al., 2022) that Mááz may be related to (Hundal et al., 2022; Sun & Stack, 2020). Although these orbital observations are conducted at a much larger, regional scale than the analyses possible with *Perseverance* data up until Sol 379, it is possible that Mááz and Séítah also drape the underlying topography. A pyroclastic fall origin could explain this draping morphology. This could also be explained by PDC processes, although such deposits would still be expected to thicken in topographic lows and thin in topographic highs (Brown & Andrews, 2015). In Gusev crater, the *Spirit* rover encountered rocks interpreted to be pyroclastic in origin (e.g., Ruff et al., 2014; Squyres et al., 2007), some of which are spectrally similar to the regional olivine-bearing unit that Séítah is hypothesized to be related to (Ruff et al., 2022). Observations of these rocks in Gusev crater included the presence of a bomb sag (Squyres et al., 2007) and fine laminations and cross-bedding in a deposit, where clast sizes were deemed too large for aeolian reworking (Lewis et al., 2008). In Jezero crater, however, we have not seen evidence of embedded larger rock fragments, pumice (i.e., frothy appearance), bomb sags, fiamme, or abundant glass within either the Séítah or Mááz formation, which disfavors a pyroclastic origin for either unit. The micro-gabbroic texture and presence of interlocking crystal grains in all Mááz and Séítah abrasion patches is also difficult to explain through a pyroclastic origin (e.g., we do not see textural evidence that the abrasion patches sampled embedded lithic inclusions in an otherwise clastic matrix, which would be consistent with a PDC deposit). However, there are some laterally fine continuous, recessive layers within the Artuby ridge of the Mááz unit which could potentially be explained by pyroclastic fall processes (see Alwmark et al., 2023).

a) Lava flow ? = Complex textures b) Pyroclastic flows ? = Draping topography

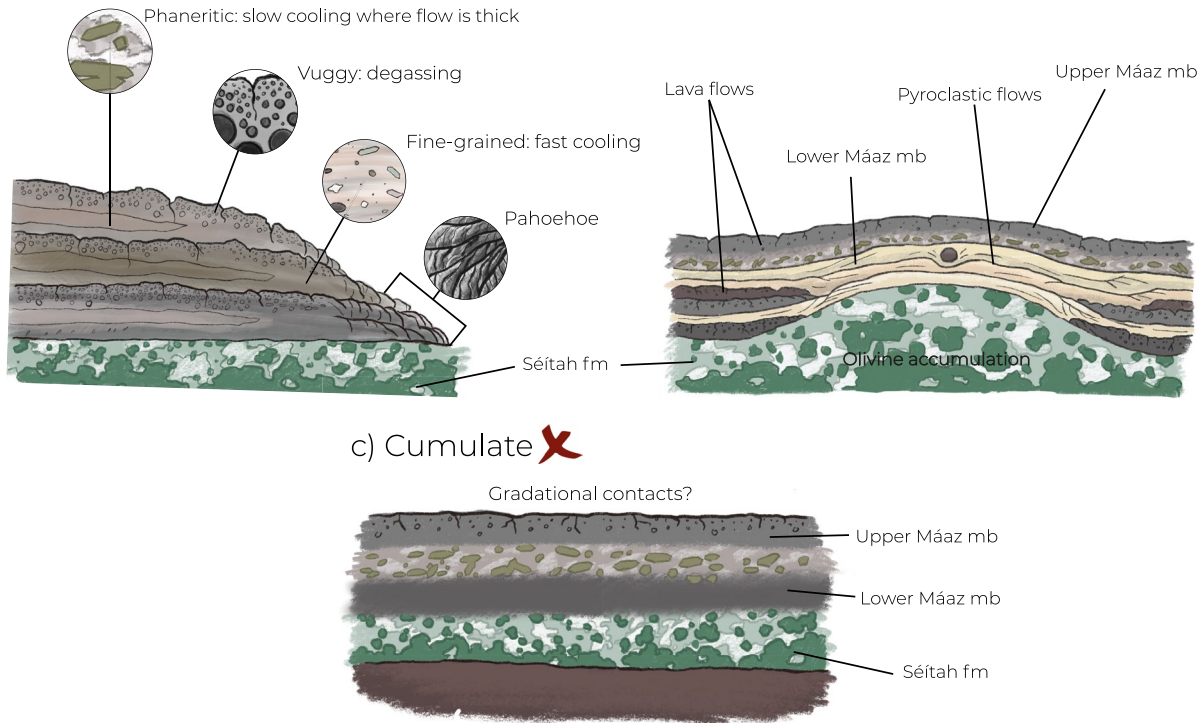


**Figure 13.** Schematics of different formation scenarios of the Máaz fm based on observed stratigraphy. We did not include the Content mb as its stratigraphy is not well constrained: (a) Lava flows displaying complex textures, including coarser-grained and fine-grained textures and vesicular and non-vesicular rocks and basaltic pāhoehoe texture all observed in the Máaz formation; (b) Pyroclastic flows: although we did not observe evidence of pyroclastic volcanism such as bombs, ash flows, and welded tuffs, fine-layered features in lower Máaz mb, we do not exclude the possibility of their presence in the lower Máaz mb; and (c) Cumulate: formed through intrusive magmatism. We discard this formation hypothesis as the Máaz fm displays effusive extrusive textures.

#### 4.6.2. Cumulate Origin

The Séítah fm was interpreted as an olivine-cumulate, based on its coarser-grained texture (possibly phaneritic) and mineral assemblage. Fine-grained and vesicular textures representing effusive volcanism are prevalent in the Máaz fm and Content mb. Thus, we exclude a cumulate origin for these members. However, this does not exclude a cumulate origin for the regional mafic cap, as the link between Máaz rocks explored by Perseverance and this regional unit has not yet been established. In addition, the Séítah and Máaz fms are likely not petrogenetically linked, as indicated by the mineralogy. Therefore, the presence of two cumulate units not petrogenetically related and stratigraphically in contact with each other, is very unlikely.

#### 4.6.3. Impact Melt

Mustard et al. (2007) proposed that the olivine-rich unit in Isidis represents an impact melt formed from the Isidis event, which would have created a large amount of melt, and could have potentially differentiated. However, Mandon et al. (2020) showed that the age gap between the olivine-rich unit and the Isidis impact event is too large, which implies that the Máaz (and Séítah) fm are not impact melt. Additionally, if the Séítah and Máaz fms are unrelated, they could not have originated from one single differentiated impact melt.

#### 4.6.4. Clastic/Aqueous Sedimentary

The bulk compositions of the rocks from the Máaz fm and Content mb and the presence of laminations in rocks from the lower Máaz mb (see Alwmark et al., 2023) indicate a possible clastic sedimentary origin. However, the fact that the different members (upper, lower Máaz members, and Content mb) show liquid evolutionary trends and pyroxene evolutionary trends all representing igneous differentiation, renders a sedimentary origin highly unlikely. In addition, the primary vesicular textures and interlocking crystal morphologies observed in

the abraded patches are consistent with igneous rocks and not sedimentary rocks (if these vesicles are indeed primary). No typical sedimentary structures (e.g., cross stratification, clasts in a matrix) have been observed. Note that clastic sedimentary rocks on Mars would be composed of high temperature igneous minerals, such as olivine, pyroxene, and plagioclase—unlike terrestrial sedimentary rocks, which primarily contain quartz, feldspar, and clay minerals.

#### 4.7. Future Analyses of Returned Máaz Samples

Four rock samples have been collected in the Máaz fm, including Montdenier (Sol 194) and Montagnac (Sol 196) from the Rochette rock and Hahonih (Sol 371) and Atsah (Sols 374/377) samples from the Sid rock (Figure 1). Montdenier and Montagnac represent the lower Máaz mb and Hahonih and Atsah representing the upper Máaz mb (Horgan et al., 2023; see Table S1 for the compositions of rocks where cores were collected). The return to Earth of these samples is crucial to constrain their formation and more broadly the igneous evolution of Mars (see Simon et al., 2022; Simon et al., 2023, for description of Máaz samples and sample analyses). The origin of the Máaz fm is not well constrained using the current tools that we have at the Martian surface, as described in the previous section. If analyzed in high-precision Earth-based laboratories, the origin of the Máaz samples could be revealed. For example, if this formation is an impact melt, then textural evidence, including shock melt/glass and shocked mineral/rock clasts, would be observable under the microscope. A high bulk abundance of platinum-group elements would also indicate an impact origin. Hand sample and microscopic textural analyses could help determine any evidence for a pyroclastic origin, and would also help assess the mineralogic phases present.

Ultra-sensitive analyses, such as trace elements and isotopic analyses of the returned Máaz fm samples, along with Séítah fm samples would help constrain their parental melts, sources compositions, and their potential links to each other and to other Martian samples, that is, meteorites. The Máaz fm rocks are different in composition (Fe-rich) and textures from the currently recovered Martian meteorites and other Martian igneous rocks, and their investigation would help decipher the diversity of the Martian interior and eruptive processes. Isotopic analyses would help elucidate the geodynamical evolution of Mars, its geochemical reservoirs, and age constraints (Simon et al., 2022; Simon et al., 2023). If the Máaz formation does indeed consist of lava flows, and the crater retention history of the upper Máaz mb can be understood the absolute dating of these samples in a high-precision Earth-based laboratory will help to anchor the Martian crater-counting calibration (Simon et al., 2022; Simon et al., 2023). The age of the Máaz fm will also help constrain the age of the volcanic activity and lacustrine activity in Jezero crater, as the Máaz fm is probably located below the delta and thus would indicate the maximum age of the lake (Quantin-Nataf et al., 2021). The investigation of the Máaz fm in Earth-based laboratories, including bulk and mineral major and trace element compositions, textures, and isotopic compositions, and comparison with all other igneous rocks from Mars (surface rocks and meteorites) would help better understand the magmatic history and evolution of the Martian interior.

## 5. Conclusions

The Máaz fm was explored by the Mars 2020 *Perseverance* rover during the first year of its traverse in Jezero crater, Mars. Data collected with the SuperCam instrument allows us to constrain the chemistry, mineralogy, and textures of these geological targets. Rocks from the upper and lower Máaz mbs and from the Content mb are undoubtedly igneous and show compositions ranging from basaltic to basaltic-andesite and basaltic trachyandesite. These rocks display some of the lowest Mg content ever reported for Martian magmatic rocks. They all have the same mineralogy and contain Fe-rich pyroxenes and fine-grained plagioclase, with possible minor minerals. We observe complex textures in the Máaz fm, with both fine-grained and mixed-sized rocks including pitted and non-pitted textures and a variety of grain-sizes, similar to lava flows on Earth. The rocks show some differences compared to other Martian magmatic rocks, including higher abundances in SiO<sub>2</sub>, FeO, and alkalis and lower Al<sub>2</sub>O<sub>3</sub>, and resemble the most evolved pyroxene-bearing basaltic shergottite Los Angeles and the gabbroic shergottite NWA 7320. According to compositions, mineralogies, and thermodynamic modeling, we infer that the upper and lower Máaz mb and Content mb are all petrogenetically linked, possibly originating from the same magmatic system that could have undergone recharges, according to our mineralogical results. However, the Máaz fm is likely not petrogenetically linked to the Séítah fm and comes from different parental magmas and/or sources. The Máaz fm and Content mb are likely lava flows and/or possibly pyroclastic flows that were emplaced

on top of the Séítah fm, as also noted by Wiens et al. (2022). Because samples of these geological members were cored and cached by the *Perseverance* rover, studies of these samples on Earth would constrain their petrogenetic links, their formation process(es?), and more broadly, help us better understand the igneous evolution of Mars.

### Data Availability Statement

The supporting information tables are available in the figshare database (Udry et al., 2022). The data in this publication are from the SuperCam, MastCam-Z, and Watson instruments, and the NavCam cameras of the Mars 2020 *Perseverance* rover. The data citations for SuperCam, MastCam-Z, and WATSON can be found in Wiens and Maurice (2021), Bell and Maki (2021), Beegle (2021). The SuperCam data include the Laser Induced Breakdown Spectroscopy (LIBS), Visible/near infrared (VISIR) Spectroscopy, and the Remote Micro-Imager (RMI). The SuperCam major element oxide composition (MOC), total emissivity, and all raw data and processed calibrated data files are included in the Planetary Data System (Wiens & Maurice, 2021). In addition, all image data presented here from the SuperCam and Mastcam-Z instruments are available through the Planetary Data System Imaging Node ([https://pds-imaging.jpl.nasa.gov/portal/mars2020\\_mission.html](https://pds-imaging.jpl.nasa.gov/portal/mars2020_mission.html)) and GeoSciences Node (<https://pds-geosciences.wustl.edu/missions/mars2020/>).

### References

- Agee, C. B., Wilson, N. V., McCubbin, F. M., Ziegler, K., Polyak, V. J., Sharp, Z. D., et al. (2013). Unique meteorite from early Amazonian Mars: Water-rich basaltic breccia Northwest Africa 7034. *Science*, 339(6121), 780–785. <https://doi.org/10.1126/science.1228858>
- Allwood, A. C., Wade, L. A., Foote, M. C., Elam, W. T., Hurowitz, J. A., Battel, S., et al. (2020). PIXL: Planetary instrument for X-ray lithochemistry. *Space Science Reviews*, 216(8), 1–132.
- Alwmark, S., Horgan, B., Udry, A., Bechtold, A., Fagents, S., Ravanis, E., et al. (2023). Diverse lava flow morphologies in the stratigraphy of the Jezero crater floor. *Journal of Geophysical Research: Planets*, 128, e2022JE007446. <https://doi.org/10.1029/2022JE007446>
- Anderson, R. B., Forni, O., Cousin, A., Wiens, R. C., Clegg, S. M., Frydenvang, J., et al. (2022). Post-landing major element quantification using SuperCam laser induced breakdown spectroscopy. *Spectrochimica Acta Part B: Atomic Spectroscopy*, 188, 106347–106357. <https://doi.org/10.1016/j.sab.2016.12.002>
- Aramovich, C. J., Herd, C. D., & Papike, J. J. (2002). Symplectites derived from metastable phases in Martian basaltic meteorites. *American Mineralogist*, 87(10), 1351–1359. <https://doi.org/10.2138/am-2002-1010>
- Balta, J. B., & McSween, H. Y. (2013). Application of the MELTS algorithm to Martian compositions and implications for magma crystallization. *Journal of Geophysical Research: Planets*, 118(12), 2502–2519. <https://doi.org/10.1002/2013JE004461>
- Baratoux, D., Toplis, M. J., Monnereau, M., & Gasnault, O. (2011). Thermal history of Mars inferred from orbital geochemistry of volcanic provinces. *Nature*, 472(7343), 338–341. <https://doi.org/10.1038/nature09903>
- Basu Sarbadhikari, A. B., Goodrich, C. A., Liu, Y., Day, J. M., & Taylor, L. A. (2011). Evidence for heterogeneous enriched shergottite mantle sources in Mars from olivine-hosted melt inclusions in Larkman Nunatak 06319. *Geochimica et Cosmochimica Acta*, 75(22), 6803–6820. <https://doi.org/10.1016/j.gca.2011.09.001>
- Beegle, L. (2021). Mars 2020 Sherlock Watson data collection. *NASA Planetary Data System*. <https://doi.org/10.17189/1522643>
- Bell, J. F., & Maki, J. M. (2021). Mars 2020 mast camera zoom bundle. *NASA Planetary Data System*. <https://doi.org/10.17189/1522843>
- Beysac, O., Forni, O., Cousin, A., Udry, A., Kah, L. C., Mandon, L., et al. (2023). Petrological traverse of the olivine cumulate Séítah formation at Jezero crater, Mars: A perspective from SuperCam onboard Perseverance. *Journal of Geophysical Research: Planets*, 128, e2022JE007638. <https://doi.org/10.1029/2022JE007638>
- Brown, A. J., Hook, S. J., Baldrige, A. M., Crowley, J. K., Bridges, N. T., Thomson, B. J., et al. (2010). Hydrothermal formation of clay-carbonate alteration assemblages in the nili fossae region of Mars. *Earth and Planetary Science Letters*, 297(1–2), 174–182. <https://doi.org/10.1016/j.epsl.2010.06.018>
- Brown, A. J., Viviano, C. E., & Goudge, T. A. (2020). Olivine-carbonate mineralogy of the Jezero crater region. *Journal of Geophysical Research: Planets*, 125(3), e2019JE006011. <https://doi.org/10.1029/2019JE006011>
- Brown, R. J., & Andrews, G. D. (2015). Deposits of pyroclastic density currents. In *The encyclopedia of volcanoes* (pp. 631–648). Academic Press.
- Clavé, E., Benzerara, K., Beck, P., Meslin, P. Y., Beysac, O., Forni, O., et al. (2022). Carbonate detection with supercam in the Jezero crater, Mars. *Lunar Planetary Science*.
- Clavé, E., Benzerara, K., Meslin, P.-Y., Forni, O., Royer, C., Mandon, L., et al. (2023). Carbonate detection with SuperCam in igneous rocks on the floor of Jezero Crater, Mars. *Journal of Geophysical Research: Planets*, 128, e2022JE007463. <https://doi.org/10.1029/2022JE007463>
- Collinet, M., Plesa, A. C., Grove, T. L., Schwinger, S., Ruedas, T., & Breuer, D. (2021). MAGMARS: A melting model for the Martian mantle and FeO-rich peridotite. *Journal of Geophysical Research: Planets*, 126(12), e2021JE006985. <https://doi.org/10.1029/2021je006985>
- Cousin, A., Sautter, V., Fabre, C., Dromart, G., Montagnac, G., Drouet, C., et al. (2022). SuperCam calibration targets on board the perseverance rover: Fabrication and quantitative characterization. *Spectrochimica Acta Part B: Atomic Spectroscopy*, 188, 106341. <https://doi.org/10.1016/j.sab.2021.106341>
- Cousin, A., Sautter, V., Payré, V., Forni, O., Mangold, N., Gasnault, O., et al. (2017). Classification of igneous rocks analyzed by ChemCam at Gale crater, Mars. *Icarus*, 288, 265–283. <https://doi.org/10.1016/j.icarus.2017.01.014>
- Crumpler, L. S., Horgan, B. H. N., Simon, J. I., Stack, K. M., Alwmark, S., Gilles, D., et al. (2023). In situ geologic context mapping transect on the floor of Jezero Crater from Mars 2020 Perseverance rover observations. *Journal of Geophysical Research: Planets*, 128, e2022JE007444. <https://doi.org/10.1029/2022JE007444>
- Dreibus, G., Wlotzka, F., Huisl, W., Jagoutz, E., Kubny, A., & Spettel, B. (2002). Chemistry and petrology of the most feldspathic shergottite: Dhofar 378. *Meteoritics and Planetary Science Supplement*, 37, A43.

- Dufek, J., Ongaro, T. E., & Roche, O. (2015). Pyroclastic density currents: Processes and models. In *The encyclopedia of volcanoes* (pp. 617–629). Academic Press.
- Fabre, C., Maurice, S., Cousin, A., Wiens, R. C., Forni, O., Sautter, V., & Guillaume, D. (2011). Onboard calibration igneous targets for the Mars Science Laboratory Curiosity rover and the Chemistry Camera laser induced breakdown spectroscopy instrument. *Spectrochimica Acta Part B: Atomic Spectroscopy*, 66(3–4), 280–289. <https://doi.org/10.1016/j.sab.2011.03.012>
- Farley, K. A., Stack, K. M., Shuster, D. L., Horgan, B. H. N., Hurowitz, J. A., Tarnas, J. D., et al. (2022). Aqueously altered igneous rocks sampled on the floor of Jezero crater, Mars. *Science*, eabo2196.
- Filiberto, J., & Dasgupta, R. (2011). Fe<sup>2+</sup>–Mg partitioning between olivine and basaltic melts: Applications to Genesis of olivine-phyric shergottites and conditions of melting in the Martian interior. *Earth and Planetary Science Letters*, 304(3–4), 527–537. <https://doi.org/10.1016/j.epsl.2011.02.029>
- Forni, O., Gaft, M., Toplis, M. J., Clegg, S. M., Maurice, S., Wiens, R. C., et al. (2015). First detection of fluorine on Mars: Implications for Gale Crater's geochemistry. *Geophysical Research Letters*, 42(4), 1020–1028. <https://doi.org/10.1002/2014gl062742>
- Fouchet, T., Reess, J. M., Montmessin, F., Hassen-Khodja, R., Nguyen-Tuong, N., Humeau, O., et al. (2022). The SuperCam infrared spectrometer for the perseverance rover of the Mars 2020 mission. *Icarus*, 373, 114773. <https://doi.org/10.1016/j.icarus.2021.114773>
- Garczyski, B. J., Bell, J. F., III, Horgan, B. H. N., Johnson, J. R., Rice, M. S., Vaughan, A., et al. (2022). Perseverance and the purple coating: A Mastcam-Z multispectral story. *Lunar Planetary Science*.
- Ghiorso, M. S., & Gualda, G. A. R. (2015). An H<sub>2</sub>O–CO<sub>2</sub> mixed fluid saturation model compatible with rhyolite-MELTS. *Contributions to Mineralogy and Petrology*, 169(6), 1–30. <https://doi.org/10.1007/s00410-015-1141-8>
- Goudge, T. A., Mustard, J. F., Head, J. W., Fassett, C. I., & Wiseman, S. M. (2015). Assessing the mineralogy of the watershed and fan deposits of the Jezero crater paleolake system, Mars. *Journal of Geophysical Research: Planets*, 120(4), 775–808. <https://doi.org/10.1002/2014je004782>
- Gualda, G. A. R., Ghiorso, M. S., Lemons, R. V., & Carley, T. L. (2012). Rhyolite-MELTS: A modified calibration of MELTS optimized for silica-rich, fluid-bearing magmatic systems. *Journal of Petrology*, 53(5), 875–890. <https://doi.org/10.1093/ptrology/egr080>
- Hamilton, V. E., & Christensen, P. R. (2005). Evidence for extensive, olivine-rich bedrock on Mars. *Geology*, 33(6), 433–436. <https://doi.org/10.1130/g21258.1>
- Herd, C. D., Walton, E. L., Agee, C. B., Muttik, N., Ziegler, K., Shearer, C. K., et al. (2017). The Northwest Africa 8159 Martian meteorite: Expanding the Martian sample suite to the early Amazonian. *Geochimica et Cosmochimica Acta*, 218, 1–26. <https://doi.org/10.1016/j.gca.2017.08.037>
- Herd, C. D. K., Borg, L. E., Jones, J. H., & Papike, J. J. (2002). Oxygen fugacity and geochemical variations in the Martian basalts: Implications for Martian basalt petrogenesis and the oxidation state of the upper mantle of Mars. *Geochimica et Cosmochimica Acta*, 66(11), 2025–2036. [https://doi.org/10.1016/s0016-7037\(02\)00828-1](https://doi.org/10.1016/s0016-7037(02)00828-1)
- Hewins, R. H., Zanda, B., Humayun, M., Nemchin, A., Lorand, J. P., Pont, S., et al. (2017). Regolith breccia Northwest Africa 7533: Mineralogy and petrology with implications for early Mars. *Meteoritics & Planetary Sciences*, 52(1), 89–124. <https://doi.org/10.1111/maps.12740>
- Hollocher, K. (2004). *CIPW norm calculation program*. Geology Department.
- Horgan, B. H. N., Anderson, R. B., Dromart, G., Amador, E. S., & Rice, M. S. (2020). The mineral diversity of Jezero crater: Evidence for possible lacustrine carbonates on Mars. *Icarus*, 339, 113526. <https://doi.org/10.1016/j.icarus.2019.113526>
- Horgan, B. H. N., Rice, M., Garczyski, B., Johnson, J., Stack-Morgan, K., Vaughan, A., et al. (2022). Mineralogy, morphology, and geochronological significance of the Máz formation and the Jezero crater floor. *Lunar Planetary Science*.
- Horgan, B. H. N., Udry, A., Rice, M., Alwmark, S., Amundsen, H. E. F., Bell, J. F. III, et al. (2023). Mineralogy, morphology, and emplacement history of the Maaz formation on the Jezero crater floor from orbital and rover observations. *Journal of Geophysical Research: Planets*, 128, e2022JE007612. <https://doi.org/10.1029/2022JE007612>
- Humayun, M., Nemchin, A., Zanda, B., Hewins, R. H., Grange, M., Kennedy, A., et al. (2013). Origin and age of the earliest Martian crust from meteorite NWA 7533. *Nature*, 503(7477), 513–516. <https://doi.org/10.1038/nature12764>
- Hundal, C. B., Mustard, J. F., Kremer, C. H., Tarnas, J. D., & Pascuzzo, A. C. (2022). The Circum-Isidis capping unit: An extensive regional ashfall deposit exposed in Jezero crater. *Geophysical Research Letters*, 49(9), e2021GL096920. <https://doi.org/10.1029/2021gl096920>
- Kremer, C. H., Mustard, J. F., & Bramble, M. S. (2019). A widespread olivine-rich ash deposit on Mars. *Geology*, 47(7), 677–681. <https://doi.org/10.1130/g45563.1>
- Lewis, K. W., Aharonson, O., Grotzinger, J. P., Squyres, S. W., Bell, J. F., III, Crumpler, L. S., & Schmidt, M. E. (2008). Structure and stratigraphy of home plate from the spirit Mars exploration rover. *Journal of Geophysical Research*, 113(E12), E12S36. <https://doi.org/10.1029/2007je003025>
- Lindsley, D. H. (1983). Pyroxene thermometry. *American Mineralogist*, 68(5–6), 477–493.
- Lindsley, D. H., Papike, J. J., & Bence, A. E. (1972). Pyroxferroite: Breakdown at low pressure and high temperature. *Lunar Science*, III, 483–485.
- Liu, Y., Chen, Y., Guan, Y., Ma, C., Rossman, G. R., Eiler, J. M., & Zhang, Y. (2018). Impact-melt hygrometer for Mars: The case of shergottite Elephant Moraine (EETA) 79001. *Earth and Planetary Science Letters*, 490, 206–215. <https://doi.org/10.1016/j.epsl.2018.03.019>
- Liu, Y., Tice, M. M., Schmidt, M. E., Treiman, A. H., Kizovski, T. V., Hurowitz, J. A., et al. (2022). An olivine cumulate outcrop on the floor of Jezero crater, Mars. *Science*, 377(6614), eabo2756. <https://doi.org/10.1126/science.abo2756>
- Mandon, L., Quantin-Nataf, C., Royer, C., Beck, P., Fouchet, T., Johnson, J. R., et al. (2023). Reflectance of Jezero crater floor: 2. Mineralogical interpretation. *Journal of Geophysical Research: Planets*, 128, e2022JE007450. <https://doi.org/10.1029/2022JE007450>
- Mandon, L., Quantin-Nataf, C., Royer, C., Beck, P., Fouchet, T., Johnson, J. R., et al. (2022). Infrared reflectance of rocks and regolith at Jezero crater: One year of SuperCam observations. *Lunar Planetary Science*.
- Mandon, L., Quantin-Nataf, C., Thollot, P., Mangold, N., Lozac'h, L., Dromart, G., et al. (2020). Refining the age, emplacement and alteration scenarios of the olivine-rich unit in the Nili Fossae region, Mars. *Icarus*, 336, 113436. <https://doi.org/10.1016/j.icarus.2019.113436>
- Manrique, J. A., Lopez-Reyes, G., Cousin, A., Rull, F., Maurice, S., Wiens, R. C., et al. (2020). SuperCam calibration targets: Design and development. *Space Science Reviews*, 216(8), 1–27. <https://doi.org/10.1007/s11214-020-00764-w>
- Maurice, S., Wiens, R. C., Bernardi, P., Caïs, P., Robinson, S., Nelson, T., et al. (2021). The SuperCam instrument suite on the Mars 2020 rover: Science objectives and Mast-Unit description. *Space Science Reviews*, 217(3), 1–108.
- McCubbin, F. M., Boyce, J. W., Srinivasan, P., Santos, A. R., Elardo, S. M., Filiberto, J., et al. (2016). Heterogeneous distribution of H<sub>2</sub>O in the Martian interior: Implications for the abundance of H<sub>2</sub>O in depleted and enriched mantle sources. *Meteoritics & Planetary Sciences*, 51(11), 2036–2060. <https://doi.org/10.1111/maps.12639>
- McCubbin, F. M., Boyce, J. W., Szabó, T., Santos, A. R., Tartèse, R., Domokos, G., et al. (2016). Geologic history of Martian regolith breccia Northwest Africa 7034: Evidence for hydrothermal activity and lithologic diversity in the Martian crust. *Journal of Geophysical Research: Planets*, 121(10), 2120–2149. <https://doi.org/10.1002/2016je005143>
- McSween, H. Y., Ruff, S. W., Morris, R. V., Bell, J. F., III, Herkenhoff, K., Gellert, R., et al. (2006). Alkaline volcanic rocks from the Columbia Hills, Gusev crater, Mars. *Journal of Geophysical Research*, 111(E9), E09S91. <https://doi.org/10.1029/2006JE002698>

- McSween, H. Y., Ruff, S. W., Morris, R. V., Gellert, R., Klingelhofer, G., Christensen, P. R., et al. (2008). Mineralogy of volcanic rocks in Gusev crater, Mars: Reconciling Mössbauer, alpha particle X-ray spectrometer, and miniature thermal emission spectrometer spectra. *Journal of Geophysical Research*, 113(E6), E06S04. <https://doi.org/10.1029/2007je002970>
- McSween, H. Y., Taylor, G. J., & Wyatt, M. B. (2009). Elemental composition of the Martian crust. *Science*, 324(5928), 736–739. <https://doi.org/10.1126/science.1165871>
- McSween, H. Y., Wyatt, M. B., Gellert, R., Bell, J. F., Morris, R. V., Herkenhoff, K. E., et al. (2006). Characterization and petrologic interpretation of olivine-rich basalts at Gusev Crater, Mars. *Journal of Geophysical Research*, 111(E2), E02S10. <https://doi.org/10.1029/2005je002477>
- Monders, A. G., Medard, E., & Grove, T. L. (2007). Phase equilibrium investigations of the Adirondack class basalts from the Gusev plains, Gusev crater, Mars. *Meteoritics & Planetary Sciences*, 42(1), 131–148. <https://doi.org/10.1111/j.1945-5100.2007.tb00222.x>
- Mustard, J. F., Poulet, F., Head, J. W., Mangold, N., Bibring, J. P., Pelkey, S. M., et al. (2007). Mineralogy of the Nili fossae region with OMEGA/Mars express data: 1. Ancient impact melt in the Isidis basin and implications for the transition from the Noachian to Hesperian. *Journal of Geophysical Research*, 112(E8), E08S03. <https://doi.org/10.1029/2006je002834>
- Nekvasil, H., Filiberto, J., McCubbin, F. M., & Lindsley, D. H. (2007). Alkalic parental magmas for the chassignites? *Meteoritics & Planetary Sciences*, 42(6), 979–992. <https://doi.org/10.1111/j.1945-5100.2007.tb01145.x>
- Nekvasil, H., McCubbin, F. M., Harrington, A., Elardo, S., & Lindsley, D. H. (2009). Linking the Chassigny meteorite and the Martian surface rock Backstay: Insights into igneous crustal differentiation processes on Mars. *Meteoritics & Planetary Sciences*, 44(6), 853–869. <https://doi.org/10.1111/j.1945-5100.2009.tb00773.x>
- Núñez, J. I., Johnson, J. R., Horgan, B. N., Rice, M. S., Vaughan, A., Tate, C., et al. (2022). Stratigraphy and mineralogy of the deposits within the Súdáh region on the floor of Jezero Crater, Mars as seen with Mastcam-Z. *Lunar Planetary Science*.
- Ostwald, A., Udry, A., Payré, V., Gazel, E., & Wu, P. (2022). The role of assimilation and fractional crystallization in the evolution of the Mars crust. *Earth and Planetary Science Letters*, 585, 117514. <https://doi.org/10.1016/j.epsl.2022.117514>
- Payré, V., Siebach, K. L., Dasgupta, R., Udry, A., Rampe, E. B., & Morrison, S. M. (2020). Constraining ancient magmatic evolution on Mars using crystal chemistry of detrital igneous minerals in the sedimentary Bradbury group, Gale crater, Mars. *Journal of Geophysical Research: Planets*, 125(8), e2020JE006467. <https://doi.org/10.1029/2020JE006467>
- Peslier, A. H., Hnatyshin, D., Herd, C. D. K., Walton, E. L., Brandon, A. D., Lapen, T. J., & Shafer, J. T. (2010). Crystallization, melt inclusion, and redox history of a Martian meteorite: Olivine-phyric shergottite Larkman Nunatak 06319. *Geochimica et Cosmochimica Acta*, 74(15), 4543–4576. <https://doi.org/10.1016/j.gca.2010.05.002>
- Quantin-Nataf, C., Holm-Alwmark, S., Lasue, J., Calef, F. J., Shuster, D., Kinch, K. M., et al. (2021). The complex exhumation history of Jezero crater floor unit. *Lunar Planetary Science*.
- Rubin, A. E., Warren, P. H., Greenwood, J. P., Verish, R. S., Leshin, L. A., Hervig, R. L., et al. (2000). Los Angeles: The most differentiated basaltic Martian meteorite. *Geology*, 28(11), 1011–1014. [https://doi.org/10.1130/0091-7613\(2000\)28<1011:LATMDB>2.0.CO](https://doi.org/10.1130/0091-7613(2000)28<1011:LATMDB>2.0.CO)
- Ruff, S. W., Hamilton, V. E., Rogers, A. D., Edwards, C. S., & Horgan, B. H. (2022). Olivine and carbonate-rich bedrock in Gusev crater and the Nili Fossae region of Mars may be altered ignimbrite deposits. *Icarus*, 380, 114974. <https://doi.org/10.1016/j.icarus.2022.114974>
- Ruff, S. W., Niles, P. B., Alfano, F., & Clarke, A. B. (2014). Evidence for a Noachian-aged ephemeral lake in Gusev crater, Mars. *Geology*, 42(4), 359–362. <https://doi.org/10.1130/g35508.1>
- Santos, A. R., Agee, C. B., McCubbin, F. M., Shearer, C. K., Burger, P. V., Tartse, R., & Anand, M. (2015). Petrology of igneous clasts in Northwest Africa 7034: Implications for the petrologic diversity of the Martian crust. *Geochimica et Cosmochimica Acta*, 157, 56–85. <https://doi.org/10.1016/j.gca.2015.02.023>
- Sautter, V., Fabre, C., Forni, O., Toplis, M. J., Cousin, A., Ollila, A. M., et al. (2014). Igneous mineralogy at Bradbury rise: The first ChemCam campaign at Gale crater. *Journal of Geophysical Research: Planets*, 119(1), 30–46. <https://doi.org/10.1002/2013je004472>
- Sautter, V., Toplis, M. J., Wiens, R. C., Cousin, A., Fabre, C., Gasnault, O., et al. (2015). In situ evidence for continental crust on early Mars. *Nature Geoscience*, 8(8), 605–609. <https://doi.org/10.1038/ngeo2474>
- Schmidt, M. E., Allwood, A., Christian, J., Clark, B., Flannery, D., Hennecke, J., et al. (2022). Highly differentiated basaltic lavas examined by PIXL in Jezero crater. *Lunar Planetary Science*.
- Shahrdad, S., Kinch, K. M., Goudge, T. A., Fassett, C. I., Needham, D. H., Quantin-Nataf, C., & Knudsen, C. P. (2019). Crater statistics on the dark-toned, mafic floor unit in Jezero Crater, Mars. *Geophysical Research Letters*, 46(5), 2408–2416. <https://doi.org/10.1029/2018gl081402>
- Simon, J. I., Amundsen, H. E. F., Beegle, L. W., Bell, J., Benison, K. C., Berger, E. L., et al. (2022). Sampling of Jezero crater Mááz formation by Mars 2020 perseverance rover. *Lunar Planetary Science*.
- Simon, J. I., Hickman-Lewis, K., Cohen, B. A., Mayhew, L. E., Shuster, D. L., Debaille, V., et al. (2023). Samples collected from the floor of Jezero Crater with the Mars 2020 Perseverance rover. *Journal of Geophysical Research: Planets*, 128, e2022JE007474. <https://doi.org/10.1029/2022JE007474>
- Squyres, S. W., Aharonson, O., Clark, B. C., Cohen, B. A., Crumpler, L., De Souza, P. A., et al. (2007). Pyroclastic activity at home plate in Gusev Crater, Mars. *Science*, 316(5825), 738–742. <https://doi.org/10.1126/science.1139045>
- Stack, K. M., Williams, N. R., Calef, F., III, Sun, V. Z., Williford, K. H., Farley, K. A., et al. (2020). Photogeologic map of the perseverance rover field site in Jezero crater constructed by the Mars 2020 science team. *Space Science Reviews*, 216(8), 217. <https://doi.org/10.1007/s11214-020-00739-x>
- Sun, V. Z., & Stack, K. M. (2020). *Geologic map of Jezero crater and the Nili Planum region, Mars*. US Geological Survey Scientific Investigations Map. <https://doi.org/10.3133/sim3464.s>
- Symes, S. J. K., Borg, L. E., Shearer, C. K., & Irving, A. J. (2008). The age of the Martian meteorite Northwest Africa 1195 and the differentiation history of the shergottites. *Geochimica et Cosmochimica Acta*, 72(6), 1696–1710. <https://doi.org/10.1016/j.gca.2007.12.022>
- Tait, K. T., & Day, J. M. (2018). Chondritic late accretion to Mars and the nature of shergottite reservoirs. *Earth and Planetary Science Letters*, 494, 99–108. <https://doi.org/10.1016/j.epsl.2018.04.040>
- Taylor, L. A., Nazarov, M. A., Shearer, C. K., McSween, H. Y., Jr., Cahill, J., Neal, C. R., et al. (2002). Martian meteorite Dhofar 019: A new shergottite. *Meteoritics & Planetary Sciences*, 37(8), 1107–1128. <https://doi.org/10.1111/j.1945-5100.2002.tb00881.x>
- Treiman, A. H., Bish, D. L., Vaniman, D. T., Chipera, S. J., Blake, D. F., Ming, D. W., et al. (2016). Mineralogy, provenance, and diagenesis of a potassic basaltic sandstone on Mars: ChemMin X-ray diffraction of the Windjana sample (Kimberley area, Gale crater). *Journal of Geophysical Research: Planets*, 121(1), 75–106. <https://doi.org/10.1002/2015je004932>
- Udry, A., Balta, J. B., & McSween, H. Y. (2014). Exploring fractionation models for Martian magmas. *Journal of Geophysical Research: Planets*, 119, 1–18. <https://doi.org/10.1002/2013JE004445>
- Udry, A., Sautter, V., Cousin, A., Wiens, R. C., Forni, O., Benzerara, K., et al. (2022). A Mars 2020 perseverance SuperCam perspective on the igneous nature of the Mááz formation at Jezero crater and link with Séítah, Mars. *Journal of Geophysical Research: Planets*. <https://doi.org/10.6084/m9.figshare.21038962>

- Udry, A., Gazel, E., & McSween, H. Y., Jr. (2018). Formation of evolved rocks at Gale crater by crystal fractionation and implications for Mars crustal composition. *Journal of Geophysical Research: Planets*, 123(6), 1525–1540. <https://doi.org/10.1029/2018JE005602>
- Udry, A., Howarth, G. H., Herd, C. D. K., Day, J. M. D., Lapen, T. J., & Filiberto, J. (2020). What Martian meteorites reveal about the interior and surface of Mars. *Journal of Geophysical Research: Planets*, 125(12), e2020JE006523. <https://doi.org/10.1029/2020je006523>
- Udry, A., Howarth, G. H., Lapen, T. J., & Richter, M. (2017). Petrogenesis of the NWA 7320 enriched Martian gabbroic shergottite: Insight into the Martian crust. *Geochimica et Cosmochimica Acta*, 204(3), 1–18. <https://doi.org/10.1016/j.gca.2017.01.032>
- Udry, A., Lunning, N. G., McSween, H. Y., Jr., & Bodnar, R. J. (2014). Petrogenesis of an impact melt clast in the Martian meteorite breccia NWA7034. *Geochimica et Cosmochimica Acta*, 141, 281–293. <https://doi.org/10.1016/j.gca.2014.06.026>
- Usui, T., Alexander, C. M. O. D., Wang, J., Simon, J. L., & Jones, J. H. (2015). Meteoritic evidence for a previously unrecognized hydrogen reservoir on Mars. *Earth and Planetary Science Letters*, 410, 140–151. <https://doi.org/10.1016/j.epsl.2014.11.022>
- Usui, T., McSween, H. Y., & Clark, B. C. (2008). Petrogenesis of high-phosphorous Wishstone class rocks in Gusev crater, Mars. *Journal of Geophysical Research*, 113(E12), 13. <https://doi.org/10.1029/2008je003225>
- Walton, E. L., Kelley, S. P., & Herd, C. D. (2008). Isotopic and petrographic evidence for young Martian basalts. *Geochimica et Cosmochimica Acta*, 72(23), 5819–5837. <https://doi.org/10.1016/j.gca.2008.09.005>
- Walton, E. L., Sharp, T. G., Hu, J., & Filiberto, J. (2014). Heterogeneous mineral assemblages in Martian meteorite Tissint as a result of a recent small impact event on Mars. *Geochimica et Cosmochimica Acta*, 140, 334–348. <https://doi.org/10.1016/j.gca.2014.05.023>
- Wiens, R. C., Maurice, S., Robinson, S. H., Nelson, A. E., Cais, P., Bernardi, P., et al. (2021). The SuperCam instrument suite on the NASA Mars 2020 rover: Body unit and combined system tests. *Space Science Reviews*, 217(1), 1–87.
- Wiens, R. C., & Maurice, S. A. (2021). *Mars 2020 SuperCam bundle*. NASA Planetary Data System. <https://doi.org/10.17189/1522646>
- Wiens, R. C., Udry, A., Beyssac, O., Quantin-Nataf, C., Mangold, N., Cousin, A., et al. (2022). Compositionally and density stratified igneous terrain in Jezero crater, Mars. *Science Advances*, 8(34), eabo3399. <https://doi.org/10.1126/sciadv.abo3399>
- Wittmann, A., Korotev, R. L., Jolliff, B. L., Irving, A. J., Moser, D. E., Barker, I., & Rumble, D., III. (2015). Petrography and composition of Martian regolith breccia meteorite Northwest Africa 7475. *Meteoritics & Planetary Sciences*, 50(2), 326–352. <https://doi.org/10.1111/maps.12425>

## References From the Supporting Information

- Balta, J. B., Sanborn, M. E., Udry, A., Wadhwa, M., & Mcsween, H. Y. (2015). Petrology and trace element geochemistry of Tissint, the newest shergottite fall. *Meteoritics & Planetary Sciences*, 50(1), 63–85. <https://doi.org/10.1111/maps.12403>
- Barrat, J. A., Jambon, A., Bohn, M., Gillet, P., Sautter, V., Göpel, C., et al. (2002). Petrology and chemistry of the picritic shergottite Northwest Africa 1068 (NWA 1068). *Geochimica et Cosmochimica Acta*, 66(19), 3505–3518. [https://doi.org/10.1016/s0016-7037\(02\)00934-1](https://doi.org/10.1016/s0016-7037(02)00934-1)
- Dunham, E. T., Balta, J. B., Wadhwa, M., Sharp, T. G., & McSween, H. Y. (2019). Petrology and geochemistry of olivine-phyric shergottites LAR 12095 and LAR 12240: Implications for their petrogenetic history on Mars. *Meteoritics & Planetary Sciences*, 25(4), 1–25. <https://doi.org/10.1111/maps.13262>
- Filiberto, J., Gross, J., Udry, A., Trela, J., Wittmann, A., Cannon, K. M., et al. (2018). shergottite Northwest Africa 6963: A pyroxene-cumulate Martian gabbro. *Journal of Geophysical Research: Planets*, 123(7), 1823–1841. <https://doi.org/10.1029/2018JE005635>
- Goodrich, C. A. (2002). Olivine-phyric Martian basalts: A new type of shergottite. *Meteoritics & Planetary Sciences*, 37(S12), B31–B34. <https://doi.org/10.1111/j.1945-5100.2002.tb00901.x>
- Gross, J., Treiman, A. H., Filiberto, J., & Herd, C. D. K. (2011). Primitive olivine-phyric shergottite NWA 5789: Petrography, mineral chemistry, and cooling history imply a magma similar to Yamato-980459. *Meteoritics & Planetary Sciences*, 46(1), 116–133. <https://doi.org/10.1111/j.1945-5100.2010.01152.x>
- Gross, J., Filiberto, J., Herd, C. D. K., Daswani, M. M., Schwenzler, S. P., & Treiman, A. H. (2013). Petrography, mineral chemistry, and crystallization history of olivine-phyric shergottite NWA 6234: A new melt composition. *Meteoritics & Planetary Sciences*, 48(5), 854–871. <https://doi.org/10.1111/maps.12092>
- He, Q., Xiao, L., Balta, J. B., Baziotis, I. P., Hsu, W., & Guan, Y. (2015). Petrography and geochemistry of the enriched basaltic shergottite Northwest Africa 2975. *Meteoritics & Planetary Sciences*, 21(12), 2024–2044. <https://doi.org/10.1111/maps.12571>
- Herd, C. D. K. (2019). Reconciling redox: Making spatial and temporal sense of oxygen fugacity variations in Martian igneous rocks. In *Lunar and planetary institute science conference L* (Vol. 2019).
- Hewins, R. H., Humayun, M., Barrat, J. A., Zanda, B., Lorand, J. P., Pont, S., et al. (2020). Northwest Africa 8694, a ferroan chassignite: Bridging the gap between nakhlites and chassignites. *Geochimica et Cosmochimica Acta*, 282, 201–226. <https://doi.org/10.1016/j.gca.2020.05.021>
- Hui, H., Peslier, A. H., Lapen, T. J., Shafer, J. T., Brandon, A. D., & Irving, A. J. (2011). Petrogenesis of basaltic shergottite Northwest Africa 5298: Closed-system crystallization of an oxidized mafic melt. *Meteoritics & Planetary Sciences*, 46(9), 1313–1328. <https://doi.org/10.1111/j.1945-5100.2011.01231.x>
- Humayun, M., Nemchin, A., Zanda, B., Hewins, R. H., Grange, M., Kennedy, A., et al. (2013). Origin and age of the earliest Martian crust from meteorite NWA 7533. *Nature*, 503(7477), 513–516. <https://doi.org/10.1038/nature12764>
- Ikeda, Y., Kimura, M., Takeda, H., Shimoda, G., Kita, N. T., Morishita, Y., et al. (2006). Petrology of a new basaltic shergottite: Dhofar 378. *Antarctic Meteorite Research*, 19, 20–44.
- Jambon, A., Barrat, J. A., Sautter, V., Gillet, P., Göpel, C., Javoy, M., et al. (2002). The basaltic shergottite Northwest Africa 856: Petrology and chemistry. *Meteoritics and Planetary Science*, 37(9), 1147–1164. <https://doi.org/10.1111/j.1945-5100.2002.tb00885.x>
- Lapen, T. J., Richter, M., Andreasen, R., Irving, A. J., Satkoski, A. M., Beard, B. L., et al. (2017). Two billion years of magmatism recorded from a single Mars meteorite ejection site. *Science Advances*, 3(2), e1600922. <https://doi.org/10.1126/sciadv.1600922>
- Ming, D. W., Mittlefehldt, D. W., Morris, R. V., Golden, D. C., Gellert, R., Yen, A., et al. (2006). Geochemical and mineralogical indicators for aqueous processes in the Columbia Hills of Gusev crater, Mars. *Journal of Geophysical Research*, 111(E2), E02S12. <https://doi.org/10.1029/2005je002560>
- Rahib, R. R., Udry, A., Howarth, G. H., Gross, J., Paquet, M., Combs, L. M., et al. (2019). Mantle source to near-surface emplacement of enriched and intermediate poikilitic shergottites in Mars. *Geochimica et Cosmochimica Acta*, 266, 463–496. <https://doi.org/10.1016/j.gca.2019.07.034>
- Santos, A. R., Agee, C. B., McCubbin, F. M., Shearer, C. K., Burger, P. V., Tartèse, R., & Anand, M. (2015). Petrology of igneous clasts in Northwest Africa 7034: Implications for the petrologic diversity of the Martian crust. *Geochimica et Cosmochimica Acta*, 157, 56–85. <https://doi.org/10.1016/j.gca.2015.02.023>
- Sautter, V., Toplis, M. J., Wiens, R. C., Cousin, A., Fabre, C., Gasnault, O., et al. (2015). In situ evidence for continental crust on early Mars. *Nature Geoscience*, 8(8), 605–609. <https://doi.org/10.1038/ngeo2474>

- Treiman, A. H. (1995). S ≠ NC: Multiple source areas for Martian meteorites. *Journal of Geophysical Research*, 100(E3), 5329. <https://doi.org/10.1029/94JE02184>
- Treiman, A. H. (2005). The nakhlite meteorites: Augite-rich igneous rocks from Mars. *Chemie Der Erde - Geochemistry*, 65(3), 203–270. <https://doi.org/10.1016/j.chemer.2005.01.004>
- Treiman, A. H., & Sutton, S. R. (1992). Petrogenesis of the Zagami meteorite: Inferences from synchrotron X-ray (SXRF) microprobe and electron microprobe analyses of pyroxenes. *Geochimica et Cosmochimica Acta*, 56(11), 4059–4074. [https://doi.org/10.1016/0016-7037\(92\)90016-c](https://doi.org/10.1016/0016-7037(92)90016-c)
- Udry, A., & Day, J. M. D. (2018). 1.34 billion-year-old magmatism on Mars evaluated from the co-genetic nakhlite and chassignite meteorites. *Geochimica et Cosmochimica Acta*, 238, 292–315. <https://doi.org/10.1016/j.gca.2018.07.006>
- Udry, A., McSween, H. Y., Hervig, R. L., & Taylor, L. A. (2016). Lithium isotopes and light lithophile element abundances in shergottites: Evidence for both magmatic degassing and subsolidus diffusion. *Meteoritics & Planetary Sciences*, 51(1), 80–104. <https://doi.org/10.1111/maps.12582>
- Usui, T., McSween, H. Y., Jr., & Floss, C. (2008). Petrogenesis of olivine-phyric shergottite Yamato 980459, revisited. *Geochimica et Cosmochimica Acta*, 72(6), 1711–1730. <https://doi.org/10.1016/j.gca.2008.01.011>
- Warren, P. H., Greenwood, J. P., & Rubin, A. E. (2004). Los Angeles: A tale of two stones. *Meteoritics & Planetary Sciences*, 39(1), 137–156. <https://doi.org/10.1111/j.1945-5100.2004.tb00054.x>
- Zipfel, J., Scherer, P., Spettel, B., Dreibus, G., & Schultz, L. (2000). Petrology and chemistry of the new shergottite Dar al Gani 476. *Meteoritics & Planetary Sciences*, 35(1), 95–106. <https://doi.org/10.1111/j.1945-5100.2000.tb01977.x>
- Zipfel, J., Schroeder, C., Jolliff, B. L., Gellert, R., Herkenhoff, K. E., Rieder, R., et al. (2011). Bounce rock—A shergottite-like basalt encountered at meridiani planum, Mars. *Meteoritics & Planetary Sciences*, 46(1), 1–20. <https://doi.org/10.1111/j.1945-5100.2010.01127.x>

## Erratum

The originally published version of this article omitted the following statement from the acknowledgments: “YL’s research was carried out at the Jet Propulsion Laboratory, California Institute of Technology, under a contract with the National Aeronautics and Space Administration (80NM0018D0004).” The statement has been added, and this version may be considered the authoritative version of record.